

# Visible-Thermal Tiny Object Detection: A Benchmark Dataset and Baselines

Xinyi Ying, Chao Xiao, Wei An, Ruojing Li, Xu He, Boyang Li, Xu Cao, Zhaoxu Li, Yingqian Wang, Mingyuan Hu, Qingyu Xu, Zaiping Lin, Miao Li, Shilin Zhou, Weidong Sheng, Li Liu

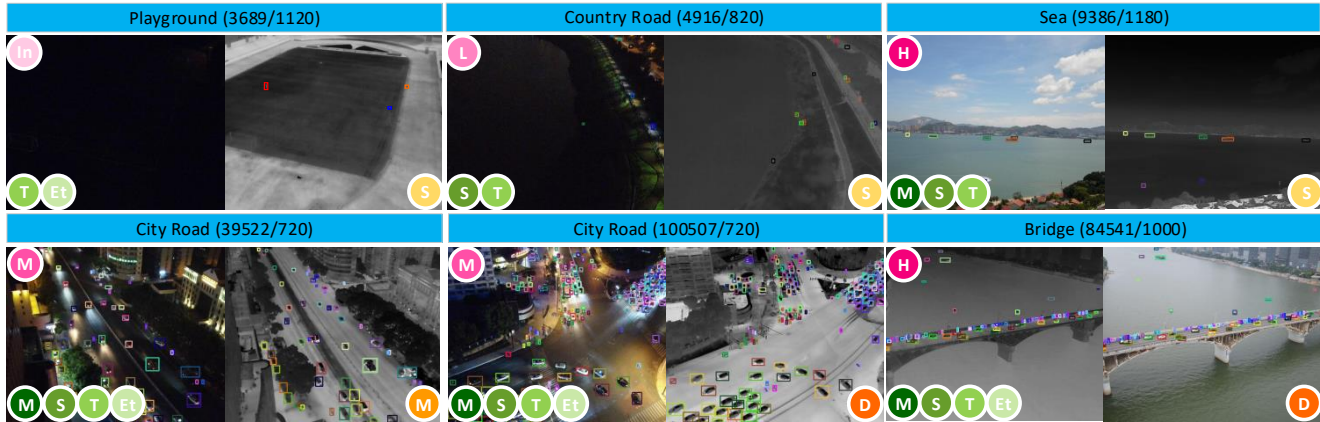


Fig. 1: Example frames of RGBT-Tiny dataset. Scenes (annotation / frame number) are shown on the top. Sequence-level attributes are shown at the bottom. Pink, green and yellow circles represent levels of light vision (i.e., H: high, M: medium, L: low, In: invisible), target size (i.e., Et: extremely tiny, T: tiny, S: small, M: medium, L: large) and annotation density (i.e., S: sparse, M: medium, D: dense).

**Abstract**—Visible-thermal small object detection (RGBT SOD) is a significant yet challenging task with a wide range of applications, including video surveillance, traffic monitoring, search and rescue. However, existing studies mainly focus on either visible or thermal modality, while RGBT SOD is rarely explored. Although some RGBT datasets have been developed, the insufficient quantity, limited diversity, unitary application, misaligned images and large target size cannot provide an impartial benchmark to evaluate RGBT SOD algorithms. In this paper, we build the first large-scale benchmark with high diversity for RGBT SOD (namely RGBT-Tiny), including 115 paired sequences, 93K frames and 1.2M manual annotations. RGBT-Tiny contains abundant objects (7 categories) and high-diversity scenes (8 types that cover different illumination and density variations). Note that, over 81% of objects are smaller than  $16 \times 16$ , and we provide paired bounding box annotations with tracking ID to offer an extremely challenging benchmark with wide-range applications, such as RGBT image fusion, object detection and tracking. In addition, we propose a scale adaptive fitness (SAFit) measure that exhibits high robustness on both small and large objects. The proposed SAFit can provide reasonable performance evaluation and promote detection performance. Based on the proposed RGBT-Tiny dataset, extensive evaluations have been conducted with IoU and SAFit metrics, including 32 recent state-of-the-art algorithms that cover four different types (i.e., visible generic detection, visible SOD, thermal SOD and RGBT object detection). Project is available at <https://github.com/XinyiYing/RGBT-Tiny>.

**Index Terms**—Visible-Thermal, Tiny Object Detection, Benchmark Dataset.

## 1 INTRODUCTION

Small objects, featured by their extremely small size (e.g., less than  $32 \times 32$  pixels [1]), are always difficult to detect. Small

- This work was supported by the National Key Research and Development Program of China No. 2021YFB3100800, the National Natural Science Foundation of China under Grant 62376283, the Science and Technology Innovation Program of Hunan Province under Grant 2021RC3069, and the Independent Innovation Science Fund Project of the National University of Defense Technology (NUDT) under Grant 22-ZZCX-042. All authors are with the College of Electronic Science and Technology, NUDT, Changsha, 410073, China. Xinyi Ying (yingxinyi18@nudt.edu.cn) and Chao Xiao (xiaochao12@nudt.edu.cn) share the equal contribution. Li Liu (liuli\_nudt@nudt.edu.cn) and Weidong Sheng (shengweidong@nudt.edu.cn) are the corresponding authors.

object detection (SOD) has received significant attention in recent years and becomes a challenging direction independent of generic object detection due to its valuable applications, including video surveillance [2–4], autonomous driving [5–7] and water rescue [8–11]. Currently, the advancement of SOD faces the following challenges. First, the extremely small size with significantly fewer appearance cues raises serious limitations for feature representation learning, whereas the complex background clutter negatively affects the detection of small objects, and can cause many false alarms. Second, the lack of large-scale, high-quality datasets greatly hinders

the advancement of SOD. Finally, the IOU-based evaluation metrics commonly used for generic object detection have a low tolerance for bounding box (bbox) perturbation of small objects and cannot guarantee high localization accuracy. Therefore, in this paper, we aim to address the aforementioned challenges to advance the development of SOD by firstly building a large-scale dataset for SOD, then developing a novel evaluation metric for SOD, and finally extensively evaluating various deep feature learning methods for SOD with the developed dataset and the proposed metric.

We build a new large-scale dataset for SOD to address the following core issues. First, most existing studies focus on either visible [2, 5, 8, 12–22] or thermal [23, 23–33] modality independently, and few research is conducted to explore the multimodal information fusion within visible-thermal (RGBT) bimodality [34–36]. Second, although various RGBT datasets [32, 34, 36–54] have been proposed, the insufficient quantity [48, 49, 53], limited diversity [37, 48, 49], unitary application [36, 48, 49], misaligned images [36, 44, 47] and large target size [38, 40, 53] cannot provide an impartial benchmark for performance evaluation on RGBT SOD. The aforementioned issues urge us to build the first large-scale benchmark with high diversity for RGBT SOD (namely RGBT-Tiny) to advance the algorithm development and piratical applications of visible SOD, thermal SOD, RGBT image fusion, RGBT small object detection and tracking.

We propose a new scale adaptive fitness (SAFit) measure to guarantee robust evaluation on both large and small objects. Specifically, SAFit performs size-aware sigmoid weighted summation between large object-friendly IoU [1] measure and small object-friendly NWD [55] measure, which can rapidly switch to an appropriate measure according to the corresponding bbox size. The switch point is flexibly controlled by a size-aware parameter  $C$  for custom requirements. In addition, a corresponding SAFit loss is developed and is demonstrated to benefit the detection performance.

Based on the proposed RGBT-Tiny dataset, we conducted extensive performance evaluations with IoU and SAFit metrics on 30 recent state-of-the-art algorithms, including visible generic detection [56–73], visible SOD [12–14], thermal SOD [24, 27, 74], and RGBT object detection [36, 48, 54, 75, 76]. Section 4.2 summarizes the challenges and effective schemes of RGBT-Tiny benchmark to lay a solid foundation for the research of RGBT SOD.

The main contributions of this paper can be summarized as follows: 1) We build the first large-scale benchmark dataset (namely RGBT-Tiny) with high diversity for RGBT SOD, including 115 paired sequences, 93K frames and 1.2M manual annotations. As compared with 32 existing benchmark datasets (including visible SOD, thermal SOD, RGBT object detection and tracking datasets), RGBT-Tiny is finely aligned, and contains abundant small objects, high diversity scenes and high-quality annotations, as shown in Fig. 1. 2) We propose a scale adaptive fitness (SAFit) measure that exhibits high robustness to both large and small objects. The proposed SAFit can provide reasonable performance evaluation, and promote detection performance when equipped during training. 3) Based on the proposed RGBT-Tiny dataset and SAFit measure,

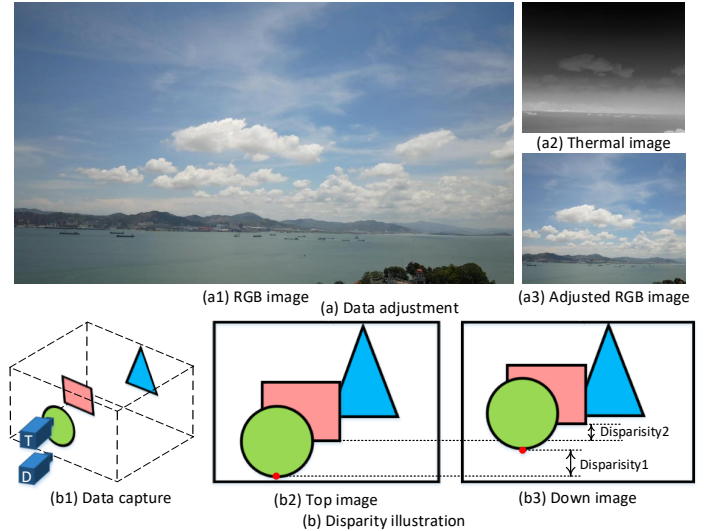


Fig. 2: (a1) Raw RGB image is aligned to (a2) thermal image to generate (a3) adjusted RGB image. (b) An illustration of disparity variations of dual lenses.

we make comprehensive evaluations on 30 current state-of-the-art algorithms, including visible generic detection, visible SOD, thermal SOD and RGBT object detection methods, which lays solid foundations for further research.

## 2 RELATED WORK

**Visible SOD.** Based on the current powerful paradigms [59, 64, 65, 68] on generic object detection, existing visible SOD methods [8, 80] introduce delicate designs tailored for small objects, including pre-processing [12, 81–83], multi-scale representation & fusion [13, 84–86], contextual information [14, 15, 87, 88] and super-resolution [89–92]. Among them, detection under low vision conditions (e.g., night, fog and rain) is rarely explored [2, 5], but is significant for practical applications [23, 37].

**Thermal SOD** performs robust on inferior illumination and weather conditions. In the past decades, numerous single-frame thermal SOD methods have been proposed, including early traditional paradigms (e.g., filtering-based [93, 94], local contrast-based [95–99], low rank-based methods [100–104]) and recent deep learning paradigms [23–25, 27, 74, 105–108]. Based on them, temporal information can be exploited [109–112] to address blur, distortion and low-contrast. However, thermal SOD fails in extreme conditions with undistinguished radiation and recognition scenes that require color and texture information.

**RGBT Object Detection** employ multimodal advantages for improved robustness. However, existing RGBT object detection methods always focus on specific tasks (e.g., pedestrian [35, 54, 113] and vehicle [36, 45, 114] detection) to explore the effective multimodal fusion [34, 35, 115–117] for spatio-temporal misalignment [35, 48, 118–121] and low light vision [35, 122, 123]. Besides these issues, RGBT SOD exhibits more challenges, including extremely small object size, fewer appearance clues, easily interfered by clutters.

TABLE 1: Statistical comparison among existing RGB SOD datasets (RGB-SOD), thermal SOD datasets (T-SOD), RGBT tracking datasets (RGBT-T), RGBT detection datasets (RGBT-D) and our RGBT-Tiny dataset. “Seq.”, “Frame”, “Anno.”, “T-Cat.” and “S-Cat.” represent the number of sequences, frames, annotations, target & scene categories, respectively. “FPS” is frame per second of released video sequences. “Split” represents the way of data split. “Align” represents whether RGBT images are aligned (Y) or not (N). “ID” represents providing tracking ID (Y) or not (N). “Pub” and “Year” represent publication name and year.

Benchmark	Seq.	Frame	Anno.	Resolution	FPS	T-Cat.	S-Cat.	Split	Align	ID	Pub	Year
RGB-SOD	SOD4SB [77]	-	39K	137K	3840×2160	-	4	4	train/test-a/test-b	-	-	CVPR 2023
	SODA-D [8]	-	24K	278K	3407×2470	-	9	-	train/val/test	-	-	TPAMI 2023
	SODA-A [8]	-	2.5K	800K	4761×2777	-	9	-	train/val/test	-	-	TPAMI 2023
	TJU-DHD Traffic [5]	-	60K	332K	1624×1200	-	5	-	train/val	-	-	TIP 2021
	SODA-10M [22]	-	10K	13K	1920×1080	-	6	-	train/val	-	-	NeurIPS 2021
	VisDrone [2]	-	40	183K	3840×2160	-	10	-	train/val/test-c/test-d	-	-	TPAMI 2021
	DOTA v2 [17]	-	11k	1.8M	800 <sup>2</sup> -4000 <sup>2</sup>	-	18	-	train/val/test-c/test-d	-	-	TPAMI 2021
	WiderPerson [16]	-	13k	400K	Varied	-	1	-	train/val/test	-	-	TMM 2020
	EuroCity Persons [21]	-	47k	211K	1920×1024	-	3	-	train/val/test	-	-	TPAMI 2020
	WiderFace [20]	-	32K	394K	Varied	-	1	61	train/val/test	-	-	CVPR 2016
MS-COCO [1]	-	328k	2.5M	Varied	-	91	-	train/val/test	-	-	ECCV 2014	
T-SOD	SIRST-v2 [78]	-	514	648	278×366	-	1	3	train/val/test	-	-	TGRS 2023
	IRSTD-1K [23]	-	1K	1.5K	512×512	-	1	6	train/val/test	-	-	CVPR 2022
	NUDT-SIRST [24]	-	1.3K	1.9K	256×256	-	1	5	train/test	-	-	TIP 2022
	IRDST [79]	401	147K	144K	795×553	-	1	-	train/test	-	-	TGRS 2023
	Fu [33]	87	22K	89K	640×512	35	1	2	train/val	-	-	CSD 2022
	SIATD [29]	350	150K	247K	640×512	30	1	3	train/test	-	-	CSD 2021
	Hui [30]	22	16K	17K	256×256	100	2	-	-	-	-	CSD 2020
RGBT-T	Anti-UAV410 [37]	410	438K	438K	640×512	25	1	7	train/val/test	N	N	TPAMI 2024
	VTUAV [41]	500	3.3M	326K	1920×1080	30	13	15	train/test	Y	N	CVPR 2022
	LasHeR [38]	1224	6.7M	6.7M	630×480	-	32	20+	train/test	Y	N	TIP 2021
	VOT-RGBT [53]	60	40K	40K	630×460	20	13	-	-	Y	N	ICCVW 2020
	RGBT234 [40]	234	234K	234K	630×460	30	22	-	-	Y	N	PR 2019
RGBT-D	DVTOD [48]	-	4.4K	12K	1920×1080	-	3	-	-	N	-	TIV 2024
	RGBTDronePerson [54]	-	16.8K	74K	640×512	-	1	-	train/test	N	-	ISPRS 2023
	M <sup>3</sup> FD [49]	-	8.4K	34K	1024×768	-	6	8	-	Y	-	CVPR 2022
	DroneVehicle [36]	-	57K	953K	840×712	-	5	-	train/val/test	N	-	TCSVT 2021
	LLVIP [43]	-	34K	-	1080×720	-	1	-	-	Y	-	ICCV 2021
	VEDAI [44]	-	1.2K	3.7K	512 <sup>2</sup> -1024 <sup>2</sup>	-	9	-	train/test	N	-	JVCI 2016
	CVC-14 [42]	4	17K	18K	640×512	10	1	-	train/test	Y	-	Sensors 2016
	KAIST [34]	41	191K	103K	640×480	20	3	-	train/test	Y	-	CVPR 2015
	FLIR [47]	7498	26K	520K	640×512	24	15	-	train/val	N	-	- 2018
	RGBT-Tiny	115	93K	1.2M	640×512	15	7	8	train/test	Y	Y	- 2024

**RGBT Datasets.** Early RGBT datasets [50–53] cannot satisfy the “data hunger” of recent deep learning-based methods due to limited quantity and category. Then large-scale datasets [32, 34, 36–49] with abundant objects & scenes and various applications have been proposed. However, the insufficient quantity [36, 42–44, 47–49, 53], limited diversity [36, 37, 42–44, 48, 49], unitary application [36–38, 40–44, 47–49, 53], misaligned images [36, 37, 44, 47, 48] and large target size [36–38, 40–44, 47–49, 53] cannot provide an impartial benchmark to evaluate RGBT SOD algorithms. The aforementioned issues urge us to build the first large-scale benchmark dataset RGBT-Tiny. Recently, Xu *et al.* [124] further developed the corresponding MOT labels to promote the research development of RGBT tiny object tracking.

**Evaluation Metrics.** Intersection over union (IoU), average precision (AP) and average recall (AR) based on bbox are widely used evaluation metrics of visible SOD [8, 80]. Based on IoU, numerous modified versions have been proposed, including generalized IoU (GIoU) [125], distance IoU (DIOU) [126] and complete-IoU (CIoU) [126]. However, these metrics focus on non-overlapping bboxes, but cannot well address the inherent problem of low tolerance for bbox perturbation.

Therefore, a novel evaluation metric tailored for SOD is absolutely necessary.

### 3 RGBT-TINY BENCHMARK

#### 3.1 Data Collection and Annotations

**Data Capture.** We employ a professional UAV DJI Mavic 2 as the data acquisition platform to ensure stable flight in extreme conditions. Vertically arranged RGBT dual lenses are equipped in UAV to collect RGBT video sequences from an altitude of 60-100 meters. The frame rate of visible and thermal cameras is 30, and we sample the video sequence to 15 frames per second (FPS) in public videos for more obvious temporal motion. Thermal camera has a wavelength of 8-14  $\mu m$ , and the image sizes between visible and thermal cameras are different (*i.e.*, 1080×1920 of RGB images and 512×640 of thermal images).

**Data Adjustment.** Camera calibration [127] is first applied to remove lens distortion in RGBT images. Then, we employ homography transformation [128] to align RGB images to thermal images since the positions of RGBT cameras are relatively fixed. To address the resolution difference between RGBT images, we crop the aligned RGB image patches that

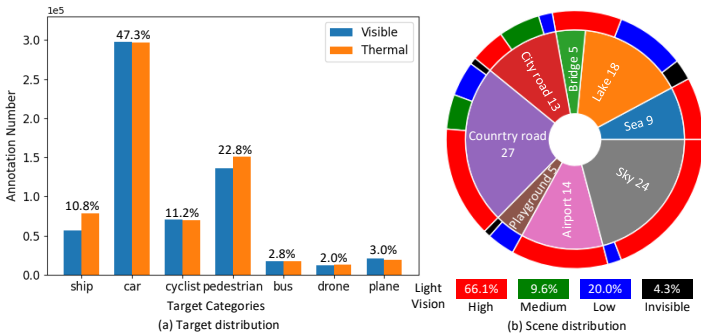


Fig. 3: (a) Annotation numbers w.r.t. target categories in visible and thermal modalities. Numbers represent the proportion of each category in annotations. (b) Inner circle shows sequence numbers w.r.t. scene categories, and outer circle shows the light vision distribution of scenes. Numbers in the pie chart represent the number of sequences of each scene type. Numbers in the legend represent the proportion of each light vision in annotations.

are consistent with thermal images to generate paired RGBT images with a resolution of  $640 \times 512$ . The adjusted RGBT images are shown in Fig. 2 (a). Note that, homography transformation can only perform frame alignment within a fixed depth of field (DoF). Therefore, the inherent disparity variation (shown in Fig. 2 (b)) of dual lenses [129] has not been well solved, and is a challenge that deserves investigation.

**Groundtruth Annotations.** We use DarkLabel [130] to annotate the groundtruth (GT) bbox with corresponding category and tracking ID. Note that, except for a few unrecognizable annotations in extreme conditions, RGBT annotations are paired within one-to-one correspondence. For quality assurance, we spent over 2000 hours conducting two-step verification. 1) Ten professional annotators make annotations respectively, and review one other annotator. 2) Each image is evaluated by another 2 assessors (5 assessors in total), and annotations are constantly revisited until without skepticism.

**Training and Test Sets.** To avoid data bias and over-fitting, training and test sets are split for 85 and 30 video sequences by the following criterion. 1) Each subset covers all types of scenes and objects. 2) Each subset covers all illumination and density variations. 3) Two subsets are not overlapped.

### 3.2 Benchmark Properties and Statistics

**Rich Diversity.** As shown in Fig. 3 (a), objects can be divided into 7 categories (e.g., ship, car, cyclist, pedestrian, bus, drone and plane). It can be observed that despite generally consistent, the number of annotations in thermal images is higher (e.g., ship and pedestrian) than those in visible images. This is because, as shown in Fig. 3 (b), our dataset covers different light visions (i.e., high-light vision is captured in the daytime, and medium-light, low-light & invisible visions are captured at night), and thermal images can provide additional supplemental information under low-light and invisible visions. Note that, night-time sequences occupy 33.9% of all data, and over 70% of them are in low-light and invisible visions. Sequences are captured at 8 types of scenes

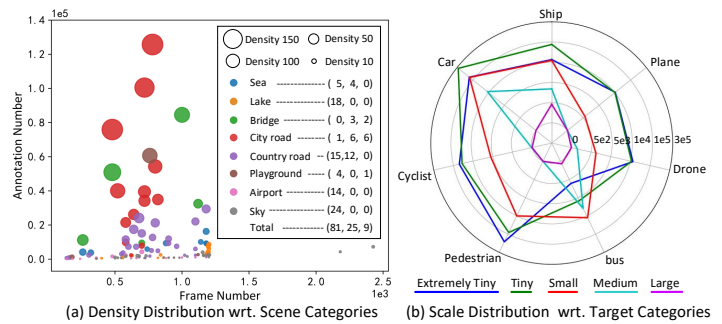


Fig. 4: (a) Average annotation number per frame (i.e., annotation density) of each sequence. Larger circle represents higher density, and different colors represent different scene types.  $(x, y, z)$  are the numbers of sequences w.r.t. density levels (i.e., sparse, medium, dense). (b) Size distribution of each target category. Lines with different colors represent different scale levels. Radius represents the annotation number, and the area under each color line represents the total annotation number of each scale level.

(e.g., sea, lake, bridge, city road, country road, playground, airport and sky) across four cities over a period of one year to obtain data in different seasons, weather and locations. Comparisons among existing datasets are listed in Table 1. In conclusion, we provide the first, large-scale, finely-aligned RGBT SOD datasets with abundant objects & scenes and high-quality annotations, which facilitates the development of RGBT image fusion, object detection and tracking.

**Large Density Variations.** Fig. 4 (a) shows the average annotation number per frame (i.e., annotation density) of each sequence, and we divide density into three levels: sparse  $\in [1, 10)$ , medium  $\in [10, 50)$ , dense  $\in [50, \infty)$ . It can be observed that our dataset covers a large range of annotation density (from 1 to 161), and density varies greatly among different scenes. Specifically, the density of city roads and bridges is much higher than that of sky and airports due to their unique objects and applications, which can provide valuable priors for object detection and recognition.

**Small-Scale Objects.** Following general scale ranks<sup>1</sup> [1], we further divide the small scale into three levels: extremely tiny  $\in [1^2, 8^2)$ , tiny  $\in [8^2, 16^2)$ , small  $\in [16^2, 32^2)$ . Fig. 4 (b) shows the annotation number with respect to (w.r.t.) the scale of each target category. It can be observed that tiny objects occupy the largest proportion (i.e., 48%) and over 97% of objects are within small or smaller scales. In addition, due to different angles (i.e., up, front and down) and distance of data acquisition, the absolute target size in image is different from the real target size. For example, larger planes are mostly divided into extremely tiny scale due to far-front handheld capture conditions, and smaller buses are mostly divided into small scale due to close-down flight capture conditions. In conclusion, objects cannot be simply classified by their absolute sizes. Comprehensive properties including appearance, context, density and motion information should be considered for accurate detection.

1. small  $\in [1^2, 32^2)$ , medium  $\in [32^2, 96^2)$  and large  $\in [96^2, \infty)$

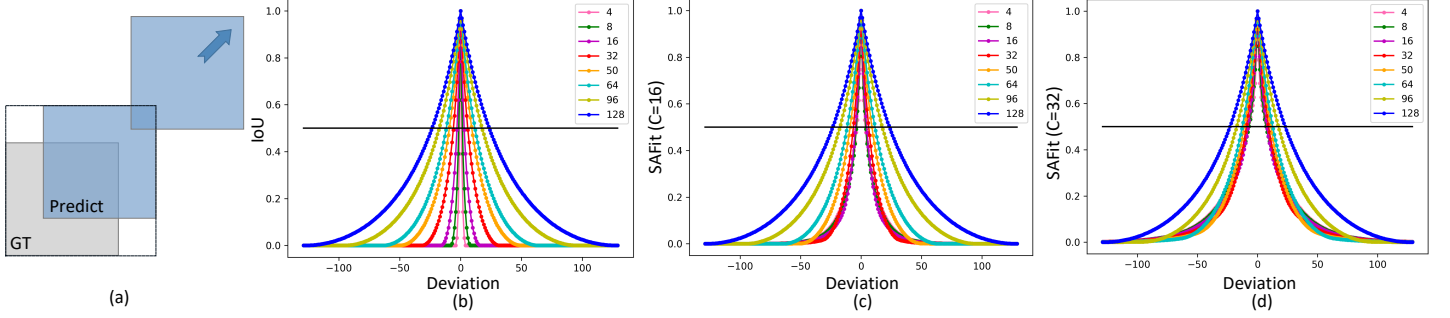


Fig. 5: (a) An illustration of the pixel deviation between the center points of GT bbox and predicted bbox. (b) IoU-Deviation curves w.r.t different sizes of bboxes. (c)-(d) SAFit-Deviation curves under different  $C$  values. The abscissa value represents the number of pixels deviation. The ordinate value represents the corresponding metric value. Note that, since the locations of bboxes can only change discretely, curves are presented as scatter diagrams.

**Temporal Occlusion.** For short-time occlusion (less than 5 frames), we employ temporal interpolation of bboxes [130, 131] to maintain consistency. For long-time occlusion (more than 5 frames), occluded frames remain unsolved. Among all annotations, 3.4% are slightly occluded (5-10 frames), 3.4% are moderately occluded (10-20 frames) and 5.2% are heavily occluded (more than 20 frames).

### 3.3 Scale Adaptive Fitness Measure

Normalized Wasserstein distance (NWD) [55] has been demonstrated to be friendly to SOD due to scale invariance and smoothness to location deviation. The formulation can be defined as:

$$\text{NWD}(K) = \exp\left(-\frac{\sqrt{W_2^2(\mathcal{N}_p, \mathcal{N}_{gt})}}{K}\right), \quad (1)$$

$$W_2^2(\mathcal{N}_p, \mathcal{N}_{gt}) = \left\| \left( \mathcal{N}_p^T, \mathcal{N}_{gt}^T \right) \right\|_2^2, \quad (2)$$

where  $W_2^2(\mathcal{N}_p, \mathcal{N}_{gt})$  is the Wasserstein distance between the Gaussian distributions of predicted bbox  $\mathcal{N}_p = [cx_p, cy_p, w_p/2, h_p/2]$  and GT bbox  $\mathcal{N}_{gt} = [cx_{gt}, cy_{gt}, w_{gt}/2, h_{gt}/2]$  with center point locations of  $(cx, cy)$ , width  $w$  and height  $h$ .  $K$  is a hyperparameter closely related to the dataset [55]. However, the scale-invariant absolute distance measure cannot provide reasonable evaluation for objects with large sizes.

Intersection over union (IoU) [80] is a common and reasonable metric for performance evaluation on large generic objects. The formulation can be defined as:

$$\text{IoU} = \frac{S_p \cap S_{gt}}{S_p \cup S_{gt}}, \quad (3)$$

where  $S_p$  and  $S_{gt}$  represent the predicted and GT bboxes. Despite scale invariance, symmetry and other advantages, IoU shows low tolerance for bbox perturbation of small objects, as shown in Fig. 5 (b). A minor location deviation (e.g., 2 pixels deviation for a small object of size  $8 \times 8$ ) can lead to a notable IoU drop (e.g., from 1 to 0.39). In conclusion, IoU-based metrics are not suitable for evaluating the performance of SOD.

To combine both advantages of IoU and NWD while avoiding drawbacks, we develop a scale adaptive fitness (SAFit) measure that exhibits high robustness to both large and

small objects. Specifically, we combine IoU and NWD via size-aware Sigmoid weighted summation:

$$\text{SAFit} = \frac{1}{1 + e^{-(\sqrt{A}/C-1)}} \times \text{IoU} + \left(1 - \frac{1}{1 + e^{-(\sqrt{A}/C-1)}}\right) \times \text{NWD}(C), \quad (4)$$

where Sigmoid function indicates a soft switch, which can rapidly switch to an appropriate measure by corresponding bbox size.  $A$  is the area of GT bbox and  $C$  is a constant that balances NWD and IoU measures in a size-aware manner. That is, when  $A = C^2$ , NWD and IoU share equal contributions. Lower value of  $A$  (i.e., smaller size of GT bbox) leads to NWD domination, while higher value results in an increased proportion of IoU. In conclusion, SAFit is practical for real applications that contain objects with varied sizes.

Quantitative comparisons among IoU and SAFit under different  $C$  values (i.e., 16, 32) are shown in Fig. 5. It can be observed that when the size of GT bbox is larger than  $C$ , SAFit is consistent with IoU. As GT bbox size decreases, SAFit rapidly turns to NWD, which is highly robust to bbox perturbation. Note that, through adjusting the value of  $C$ , SAFit can provide flexible applications for different custom requirements. For our dataset, we set  $C = 32$  because small target is defined to be smaller than  $32 \times 32$ . In addition, we develop SAFit loss (i.e.,  $L_{\text{SAFit}} = 1 - \text{SAFit}$ ) for network training, which can provide stable and accurate optimization guidance on objects with varied sizes. Note that, each component (i.e., IoU and NWD) of SAFit loss can be flexibly replaced by new measures.

## 4 EXPERIMENTS

### 4.1 Scale Adaptive Fitness Measure

**SAFit Measure for Evaluation.** We employ IoU, NWD and SAFit measures for performance evaluation on Cascade RCNN [61] in visible modality. More results are listed in supplemental material. As shown in Fig. 6 (a), AP values of SAFit are closer to those of NWD when GT bbox size is small, and rapidly switch to those of IoU as size increases. In conclusion, SAFit shows comprehensively reasonable evaluations on both large and small objects. To this end, all experimental results below are evaluated under SAFit measure if not specified.

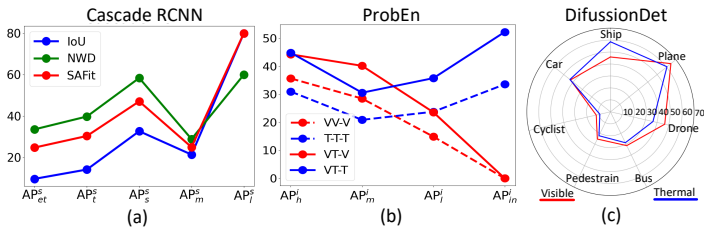


Fig. 6: (a) shows comparisons among different measures for performance evaluation.  $AP_{et}^s$ ,  $AP_t^s$ ,  $AP_s^s$ ,  $AP_m^s$ ,  $AP_l^s$  represent AP values of extremely tiny, tiny, small, medium, large objects. (b) investigates the influences of RGBT fusion. “VV”, “TT”, “VT” represent model with duplicated visible, duplicated thermal and RGBT inputs. “-V”, “-T” represent visible, thermal labels for training and test.  $AP_h^i$ ,  $AP_m^i$ ,  $AP_l^i$ ,  $AP_{in}^i$  represent AP values under high-light, medium-light, low-light, invisible illumination conditions. (c) shows performance comparisons of different classes.

**SAFit Loss for Training.** We equip different losses (*i.e.*, IoU [80], DIoU [126], CIoU [126], GIoU [125], NWD [55] and SAFit losses) with different detectors (*i.e.*, ATSS [66], SparseRCNN [69], and train the network under the same settings in visible modality. Note that, we employ 2 variants of SAFit loss (*i.e.*, SAFit-s and SAFit<sub>g</sub>) to investigate the performance of direct transition (*i.e.*, loss function is set to NWD when GT bbox size is smaller than  $C$ , while set to IoU vice versa) and stronger component (*i.e.*, Sigmoid weighted summation of GIoU and NWD). SAFit-based results are shown in Table 2. Please refer to supplemental material for corresponding IoU-based results. It can be observed that SAFit loss shows high robustness to different detectors under SAFit and IoU metrics. Compared with SAFit, SAFit-s performs inferior while SAFit<sub>g</sub> achieves improved performance, which demonstrates the superiority and flexibility of SAFit. Furthermore, SAFit<sub>g</sub> and SAFit achieve higher values compared with their components, which demonstrates that SAFit can not only combine both advantages of their components but also produce a breakthrough by offering more stable and smooth training for objects with varied sizes.

## 4.2 Baseline Results

We conduct comprehensive evaluations on 30 recent state-of-the-art detection methods, including 18 visible generic object detection methods<sup>2</sup> (*e.g.*, SSD [56], YOLO [57], TOOD [58], Faster RCNN [59], SABL [60], Cascade RCNN [61], Dynamic RCNN [62], RetinaNet [63], CenterNet [64], FCOS [65], ATSS [66], VarifocalNet [67], Deformable DETR [68] Sparse RCNN [69], CO-DETR [70], DiffusionDet [71], DINO [72] and DDQ [73]), 3 visible SOD methods<sup>3</sup> (*e.g.*, RFLA [12], QueryDet [13], C3Det [14]), 3 thermal SOD methods<sup>4</sup> (*e.g.*, ACM [27], ALCNet

2. All models are implemented by mmdetection code library [132] under their default parameters (ResNet50 [133] and FPN [84]) are preferred as the backbone and neck) and training settings. We reduce the initial anchor size of two-stage methods to adapt to small objects.

3. All models are implemented by their officially public codes.

4. All models are implemented by BasicIRSTD code library [134] under their default settings.

TABLE 2: SAFit-based results of different losses equipped with different detectors. SAFit-s, SAFit<sub>g</sub> are used to investigate the effect of direct transition (*i.e.*, loss function is set to NWD when GT bbox size is smaller than  $C$ , while set to IoU vice versa) and stronger components (*i.e.*, Sigmoid weighted summation of GIoU and NWD).

Loss	ATSS						Sparse RCNN							
	AP	AP <sub>50</sub>	AP <sub>et</sub> <sup>s</sup>	AP <sub>t</sub> <sup>s</sup>	AP <sub>s</sub> <sup>s</sup>	AP <sub>m</sub> <sup>s</sup>	AP <sub>l</sub> <sup>s</sup>	AP	AP <sub>50</sub>	AP <sub>et</sub> <sup>s</sup>	AP <sub>t</sub> <sup>s</sup>	AP <sub>s</sub> <sup>s</sup>	AP <sub>m</sub> <sup>s</sup>	AP <sub>l</sub> <sup>s</sup>
GIoU [125]	24.2	38.1	19.6	23.6	43.8	27.5	65.0	19.2	29.8	18.8	19.5	33.4	14.9	40.1
DIoU [126]	23.6	37.5	19.2	23.1	43.6	28.2	80.0	19.1	29.7	19.7	18.5	33.9	14.7	60.1
CIoU [126]	24.2	39.1	19.6	24.2	42.6	29.0	65.0	20.0	30.6	19.5	19.0	33.9	14.8	80.1
IoU [1]	23.3	37.3	19.3	23.7	42.3	26.5	75.0	8.1	14.7	11.3	7.1	11.8	0.2	0.0
NWD [55]	24.1	38.6	19.6	23.6	44.2	27.0	60.0	19.7	30.2	19.7	18.4	35.8	15.2	50.0
SAFit-s	24.3	39.0	19.7	24.3	42.1	27.5	60.0	19.8	31.2	18.4	19.4	35.5	14.5	50.1
SAFit	24.5	39.2	19.7	25.1	43.5	28.0	60.1	21.4	32.2	20.4	20.5	36.3	14.5	15.0
SAFit <sub>g</sub>	24.7	39.3	20.6	23.6	44.4	27.5	70.0	22.0	34.0	22.2	19.5	34.9	16.3	15.0

[74], DNA-Net [24]) and 6 RGBT detection methods<sup>3</sup> (*e.g.*, UA-CMDet [36], ProbEn-early [75], ProbEn-middle [75], QFDet [54], CALNet [76], CMA-Det [48]). SAFit-based results are shown in tables 3, and IoU-based results are listed in the supplemental material. Note that, all models are re-trained and evaluated on RGBT-Tiny dataset for fair comparisons.

Thermal SOD methods can only perform foreground and background segmentation. For performance evaluation on multi-category bboxes, we first enlarge the output channels of CNN-based thermal SOD models to perform multi-category segmentation. Then we employ uniform and Gaussian distribution to generate hard (*i.e.*, all pixels in bboxes are assigned to be positive pixels) and soft (*i.e.*, pixels in bboxes are assigned to probability values under Gaussian distribution [55]) mask annotations of each category for training. For test, we transfer the mask-based results to bbox-based results via the minimum enclosing rectangle of each connected region. From the results of Table 3, Soft masks can offer stable training for reasonable evaluation results, and thus breakthrough the evaluation gap between visible and thermal SOD methods.

Experimental results in Table 3 indicate some effective paradigms. 1) End-to-end detection frameworks exhibit significant advancement, including CNN-based detectors [69, 135], DETR-based detectors [68, 70, 72, 73], Diffusion-based detectors [71]. Due to insufficient appearance cues, dense proposals (*e.g.*, anchor-based [59, 61], anchor-free [64, 65], query-based [68, 73]) is more friendly to RGBT-Tiny benchmark. In addition, some technologies (*e.g.*, denoising-based location regression [71, 72] and contrastive sample balance [72, 73]) show great potential. 2) Small object-specific paradigms demonstrate promising prospects, including region proposal refinement [12, 60, 61], multi-scale information fusion [13, 14, 68] and contextual information utilization [13, 14, 54]. 3) RGBT detection methods can make full use of RGBT complementary information for performance improvements in both modalities, as shown in Table 3 and Fig. 6 (b). Among them, illumination awareness [36], misalignment robustness [48, 75] and semantic-modulation [36, 54] can well address the cross-modal semantic conflicts for superior performance. 4) Multi-dimension information (*e.g.*, appearance [61, 68], context [13, 14, 54], motion [75, 124]) integration benefits the recognition accuracy.

Compared with other public benchmarks [1, 2, 23, 24, 27, 41, 54], RGBT-Tiny is an extremely challenging benchmark. 1)

TABLE 3: SAFit-based results of existing visible generic detection (V-D), visible SOD (V-SOD), thermal SOD (T-SOD), RGBT detection methods (RGBT-D) methods on RGBT-Tiny dataset. “#Param.” represents the number of parameters. “(-)” represents network trained under replicated visible or thermal inputs to investigate the influence of multimodal fusion. Note that, the results of T-SOD are trained with hard (left) and soft (right) masks generated by bboxes under uniform and Gaussian distributions.

	Methods	#Param.	Visible										Thermal							
			AP	AP <sub>50</sub>	AP <sub>75</sub>	AP <sub>et</sub> <sup>s</sup>	AP <sub>t</sub> <sup>s</sup>	AP <sub>s</sub> <sup>s</sup>	AP <sub>m</sub> <sup>s</sup>	AP <sub>l</sub> <sup>s</sup>	AR	AP	AP <sub>50</sub>	AP <sub>75</sub>	AP <sub>et</sub> <sup>s</sup>	AP <sub>t</sub> <sup>s</sup>	AP <sub>s</sub> <sup>s</sup>	AP <sub>m</sub> <sup>s</sup>	AP <sub>l</sub> <sup>s</sup>	AR
V-D	SSD [56]	25.2M	28.0	43.1	31.9	24.2	26.6	41.9	22.7	45.0	36.8	27.0	42.0	31.8	20.2	29.5	45.7	34.8	30.0	35.9
	YOLO [57]	61.5M	24.3	37.7	28.4	21.4	25.1	35.8	20.5	60.1	30.5	24.1	36.7	28.4	18.5	29.5	40.2	26.3	50.0	30.9
	TOOD [58]	31.8M	27.9	43.5	31.7	23.1	27.9	44.6	30.6	60.0	38.6	27.9	42.3	32.0	22.1	27.9	47.9	27.7	70.0	38.9
	ATSS [66]	31.9M	24.2	38.1	26.8	19.6	23.6	43.8	27.5	65.0	38.0	27.5	42.1	32.3	19.9	29.7	46.5	44.1	80.0	40.0
	RetinaNet [63]	36.2M	21.8	37.4	22.9	20.9	19.4	34.9	25.3	75.0	34.5	19.3	32.4	21.7	15.4	21.4	33.8	35.7	80.0	35.1
	Faster RCNN [59]	41.2M	28.8	43.1	33.5	24.3	30.1	44.2	22.0	65.0	37.2	29.5	43.0	36.2	21.9	35.2	45.0	41.4	80.0	36.4
	Cascade RCNN [61]	68.9M	30.1	44.2	35.8	24.8	30.4	47.1	25.0	80.0	37.4	30.0	44.2	34.9	24.7	29.8	46.6	25.8	<u>90.0</u>	37.4
	Dynamic RCNN [62]	41.2M	29.4	44.0	34.2	24.4	31.2	45.9	23.8	55.0	37.0	28.4	40.9	34.4	21.7	33.8	47.1	40.8	60.0	35.8
	SABL [60]	41.9M	29.6	43.3	35.3	24.0	31.0	46.6	25.5	77.6	37.1	29.3	42.2	35.7	21.8	34.8	47.2	42.6	<u>90.0</u>	36.6
	CenterNet [64]	14.4M	17.8	31.7	18.2	16.7	18.4	29.4	16.4	25.0	28.9	15.5	27.3	16.2	12.2	17.7	25.7	28.5	30.0	28.2
	FCOS [65]	31.9M	17.5	28.6	19.2	15.3	18.8	32.4	20.0	45.2	30.1	16.9	27.7	19.2	14.0	17.4	38.6	29.0	<u>90.0</u>	31.2
	VariFocalNet [67]	32.5M	26.9	41.6	30.1	22.1	27.8	45.0	27.9	80.0	39.1	30.4	45.8	36.5	20.2	34.7	51.4	<u>46.8</u>	<u>90.0</u>	40.6
	Deformable DETR [68]	39.8M	28.2	45.4	32.0	25.2	27.2	43.5	22.9	65.0	38.5	28.0	44.2	32.7	21.4	31.6	48.1	37.6	70.0	38.8
	Sparse RCNN [69]	44.2M	19.2	29.8	21.9	18.8	19.5	33.4	14.9	40.1	33.7	20.6	31.5	24.0	18.0	22.4	31.6	31.0	40.0	36.1
	CO-DETR[70]	65.2M	<u>35.0</u>	52.0	40.9	<u>29.1</u>	35.7	48.5	<u>34.8</u>	85.0	<u>48.6</u>	<u>35.0</u>	49.9	<u>42.3</u>	25.0	<b>40.1</b>	51.2	<b>48.8</b>	<b>100.0</b>	<u>49.1</u>
	DiffusionDet[71]	151.0M	<b>38.4</b>	<b>55.7</b>	<b>45.5</b>	<b>34.1</b>	<u>36.4</u>	<b>53.5</b>	30.6	85.0	<b>50.4</b>	<b>36.9</b>	<b>53.4</b>	<b>44.1</b>	<b>29.5</b>	<u>39.9</u>	<b>57.5</b>	46.7	<u>90.0</u>	<b>50.8</b>
	DINO[72]	97.7M	34.7	<u>52.4</u>	<u>41.3</u>	27.6	<b>38.6</b>	<u>52.9</u>	<b>45.1</b>	<u>90.0</u>	<b>50.4</b>	34.0	50.6	41.0	25.7	37.0	53.0	44.4	80.0	48.4
DDQ[73]	48.3M	31.5	47.8	37.0	26.1	31.2	48.9	34.1	85.0	47.9	34.3	49.4	41.7	<u>26.4</u>	37.2	<u>55.0</u>	46.0	<u>90.0</u>	50.0	
V-SOD	QueryDet [13]	39.4M	23.6	36.0	28.1	19.2	25.1	37.0	20.3	30.0	37.6	25.1	39.4	30.0	19.3	31.0	40.1	21.3	40.0	39.9
	RFLA [12]	36.3M	32.1	47.1	36.3	26.8	30.4	45.3	29.4	50.0	43.0	33.8	50.2	40.1	27.5	37.6	49.8	38.8	60.0	45.4
	C3Det [14]	55.3M	9.4	13.8	11.2	0.5	8.1	42.1	25.6	81.7	10.9	11.4	16.8	13.3	0.3	8.0	48.7	45.2	80.0	13.3
T-SOD	ACM [27]	<b>0.4M</b>	1.2	2.4	1.0	8.8	5.7	5.0	0.0	0.0	4.9	18.2	32.0	20.5	21.7	25.0	22.1	11.4	40.0	24.3
	ALCNet [74]	<b>0.4M</b>	2.0	5.7	0.5	19.6	9.3	2.0	0.0	0.0	8.6	12.2	22.0	11.9	13.9	15.3	17.8	7.2	19.3	22.0
	DNA-Net [24]	<u>4.7M</u>	2.6	4.8	2.5	1.0	4.4	6.2	14.5	0.0	8.3	13.6	22.0	15.1	14.9	13.8	31.3	14.3	0.0	27.7
RGBT-D	UA-CMDet (-) [36]	139.2M	18.4	30.2	20.4	11.7	22.5	41.8	21.0	52.1	24.3	24.4	37.9	29.7	14.1	20.9	47.2	42.5	20.3	31.3
	UA-CMDet [36]	139.2M	16.1	30.6	15.6	12.1	18.5	32.7	16.9	14.2	26.2	20.0	35.0	21.4	10.8	24.1	35.0	38.5	9.7	28.5
	ProbEn-early [75]	60.3M	18.4	28.3	22.4	14.5	22.0	32.1	19.5	80.0	23.5	17.0	26.8	19.4	12.3	20.2	32.3	22.2	76.7	22.2
	ProbEn-middle (-) [75]	120.6M	24.7	35.0	29.9	20.7	24.8	38.1	26.9	85.0	29.9	26.0	36.1	32.3	19.2	31.4	40.9	35.8	80.0	31.5
	ProbEn-middle [75]	120.6M	27.4	39.7	33.4	23.4	29.6	37.2	30.8	<b>92.5</b>	33.1	29.3	41.0	35.9	21.8	35.3	44.1	37.5	70.0	34.0
	QFDet [54]	60.3M	31.8	50.0	37.5	28.1	32.6	46.4	25.2	72.5	45.3	33.2	50.3	39.3	24.3	37.5	50.9	40.6	<b>100.0</b>	43.0
	CALNet [76]	153.6M	27.5	49.4	27.1	27.1	30.5	38.8	10.3	5.0	37.3	29.4	<u>50.7</u>	30.7	25.0	35.7	44.7	24.9	5.2	38.2
CMA-Det [48]	33.4M	18.9	40.9	16.4	19.9	19.1	27.2	12.9	54.7	35.2	18.4	<u>36.0</u>	16.6	17.1	21.4	23.1	24.6	70.0	31.0	

Extremely tiny object size with significantly fewer appearance cues raises serious limitations for feature representation learning, and thus results in high miss detection and false alarm, as shown in Fig. 7 (a). 2) Cross-modal semantic conflicts, spatio-temporal misalignment and low light vision always lead to severe multimodal fusion errors and significant performance drop, as shown in Fig. 7 (b), (c). 3) Inter-class homogeneity and intra-class variations cause semantic ambiguity for limited recognition performance, as shown in Figs. 7 (d), (e). 4) Class imbalance leads to training bias, resulting in limited performance on category with fewer instances (e.g., bus, cyclist), as shown in Fig. 6 (c). Besides the aforementioned challenges, more failure cases primarily stem from severe occlusions (shown in Fig. 7 (f)), illumination variations (shown in Fig. 7 (g)), complex background clutter (shown in Figs. 7 (h1), (h2)). Please refer to supplemental material for detailed discussions of failure cases and potential solutions.

## 5 CONCLUSION

In this paper, we build the first large-scale benchmark dataset (namely RGBT-Tiny) for RGBT-SOD. RGBT-Tiny is an extremely challenging benchmark that contains abundant objects and diverse scenes, and spans over large application

scopes, including RGBT image fusion, object detection and tracking. In addition, we propose a scale adaptive fitness measure (SAFit) that exhibits high robustness to both large and small objects, which can provide reasonable performance evaluation and optimal training process. Based on the proposed RGBT-Tiny dataset, we make comprehensive evaluations on 32 recent state-of-the-art detection algorithms with IoU and SAFit metrics, and summarize the challenges and effective schemes. In future work, we aim to further enlarge the data quantity, refine the annotations, build the foundation model, exploit the temporal information and explore weakly-supervised and unsupervised RGBT SOD.

## REFERENCES

- [1] T.-Y. Lin *et al.*, “Microsoft coco: Common objects in context,” in *ECCV*, 2014.
- [2] P. Zhu *et al.*, “Detection and tracking meet drones challenge,” *TPAMI*, 2021.
- [3] Zhao, Jian *et al.*, “Towards pose invariant face recognition in the wild,” in *CVPR*, 2018.
- [4] Zhao, Jian *et al.*, “3d-aided dual-agent gans for unconstrained face recognition,” *TPAMI*, 2018.
- [5] Y. Pang *et al.*, “Tju-dhd: A diverse high-resolution dataset for object detection,” *TIP*, 2020.

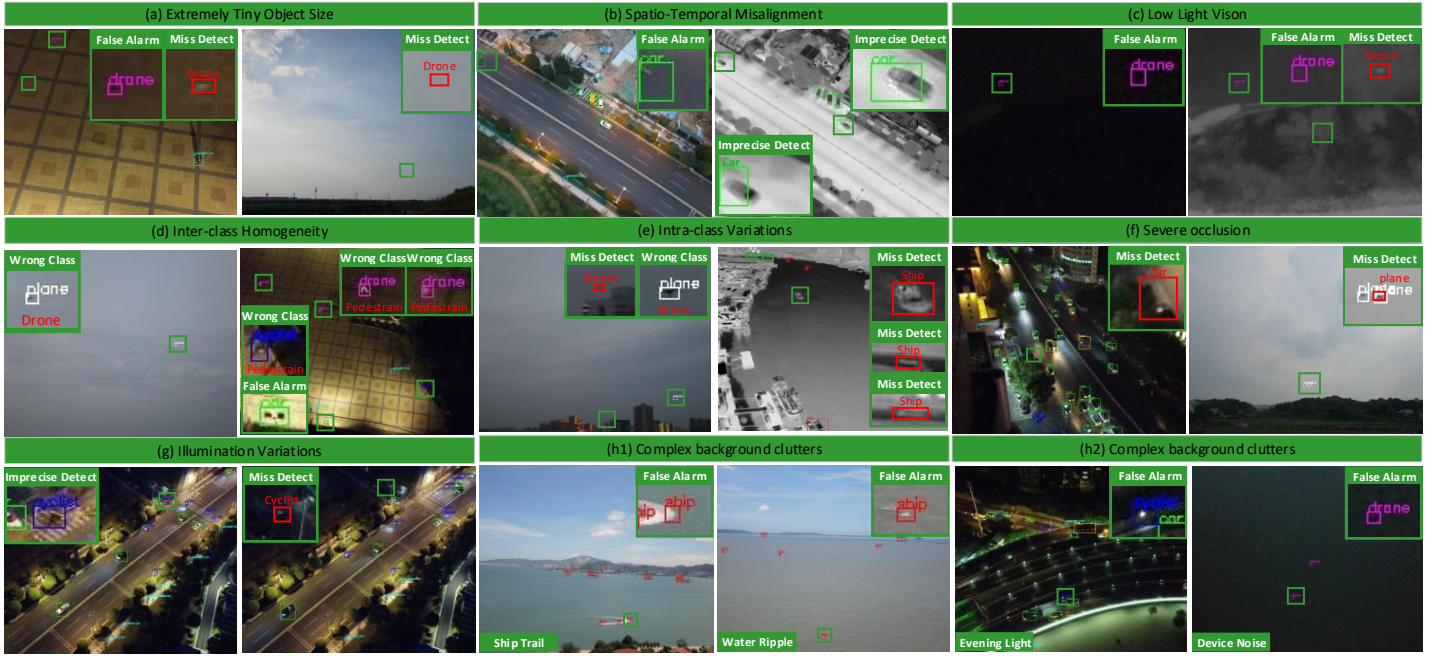


Fig. 7: Examples of challenging scenes. Green boxes show the zoom-in target regions. Red boxes & texts inside represent GT bboxes and categories.

- [6] Zhao, Jian *et al.*, "Dual-agent gans for photorealistic and identity preserving profile face synthesis," *NeurIPS*, 2017.
- [7] Zhao, Jian *et al.*, "Look across elapse: Disentangled representation learning and photorealistic cross-age face synthesis for age-invariant face recognition," *AAAI*, 2019.
- [8] G. Cheng *et al.*, "Towards large-scale small object detection: Survey and benchmarks," *TPAMI*, 2023.
- [9] Zhao, Jian *et al.*, "Towards age-invariant face recognition," *TPAMI*, 2020.
- [10] Zhao, Jian *et al.*, "3d-aided deep pose-invariant face recognition," in *IJCAI*, 2018.
- [11] Q. Wang *et al.*, "Face.evolve: A cross-platform library for high-performance face analytics," *Neurocomputing*, 2022.
- [12] C. Xu *et al.*, "Rfla: Gaussian receptive based label assignment for tiny object detection," in *ECCV*, 2022.
- [13] C. Yang *et al.*, "Querydet: Cascaded sparse query for accelerating high-resolution small object detection," in *CVPR*, 2022.
- [14] C. Lee *et al.*, "Interactive multi-class tiny-object detection," in *CVPR*, 2022.
- [15] F. C. Akyon *et al.*, "Slicing aided hyper inference and fine-tuning for small object detection," *ICIP*, 2022.
- [16] S. Zhang *et al.*, "Widerperson: A diverse dataset for dense pedestrian detection in the wild," *TMM*, 2019.
- [17] J. Ding *et al.*, "Object detection in aerial images: A large-scale benchmark and challenges," *TPAMI*, 2021.
- [18] C. Chen *et al.*, "R-cnn for small object detection," in *ACCV*, 2017.
- [19] X. Yu *et al.*, "Scale match for tiny person detection," in *WACV*, 2020.
- [20] S. Yang *et al.*, "Wider face: A face detection benchmark," in *CVPR*, 2016.
- [21] M. Braun *et al.*, "Eurocity persons: A novel benchmark for person detection in traffic scenes," *TPAMI*, 2019.
- [22] J. Han *et al.*, "Soda10m: A large-scale 2d self/semi-supervised object detection dataset for autonomous driving," *NeurIPS*, 2021.
- [23] M. Zhang *et al.*, "Isnet: Shape matters for infrared small target detection," in *CVPR*, 2022.
- [24] B. Li *et al.*, "Dense nested attention network for infrared small target detection," *TIP*, 2022.
- [25] H. Wang *et al.*, "Miss detection vs. false alarm: Adversarial learning for small object segmentation in infrared images," in *ICCV*, 2019.
- [26] C. Gao *et al.*, "Infrared patch-image model for small target detection in a single image," *TIP*, 2013.
- [27] Y. Dai *et al.*, "Asymmetric contextual modulation for infrared small target detection," in *WACV*, 2021.
- [28] T. Wu *et al.*, "Mtu-net: Multi-level transunet for space-based infrared tiny ship detection," *ArXiv*, 2022.
- [29] X. Sun *et al.*, "A dataset for small infrared moving target detection under clutter background," *CSD*, 2021.
- [30] B. Hui *et al.*, "A dataset for infrared detection and tracking of dim-small aircraft targets under ground / air background," *CSD*, 2020.
- [31] M. Zhao *et al.*, "Tbc-net: A real-time detector for infrared small target detection using semantic constraint," *ArXiv*, 2019.
- [32] N. Jiang *et al.*, "Anti-uav: a large-scale benchmark for vision-based uav tracking," *TMM*, 2021.
- [33] R. Fu *et al.*, "A dataset for infrared time-sensitive target detection and tracking for air-ground application," *CSD*, 2022.
- [34] S. Hwang *et al.*, "Multispectral pedestrian detection: Benchmark dataset and baseline," in *CVPR*, 2015.
- [35] K. Zhou *et al.*, "Improving multispectral pedestrian detection by addressing modality imbalance problems," in *ECCV*, 2020.
- [36] Y. Sun *et al.*, "Drone-based rgb-infrared cross-modality vehicle detection via uncertainty-aware learning," *TCSVT*, 2022.
- [37] B. Huang *et al.*, "Anti-uav410: A thermal infrared benchmark and customized scheme for tracking drones in the wild," *TPAMI*, 2023.
- [38] C. Li *et al.*, "Lasher: A large-scale high-diversity benchmark for rgb-t tracking," *TIP*, 2021.
- [39] C. Li *et al.*, "Weighted sparse representation regularized graph learning for rgb-t object tracking," in *ACM MM*, 2017.

- [40] C. Li *et al.*, "Rgb-t object tracking: Benchmark and baseline," *PR*, 2019.
- [41] P. Zhang *et al.*, "Visible-thermal uav tracking: A large-scale benchmark and new baseline," in *CVPR*, 2022.
- [42] A. González *et al.*, "Pedestrian detection at day/night time with visible and fir cameras: A comparison," *Sensors*, 2016.
- [43] X. Jia *et al.*, "Llvip: A visible-infrared paired dataset for low-light vision," in *ICCV*, 2021.
- [44] S. Razakarivony *et al.*, "Vehicle detection in aerial imagery: A small target detection benchmark," *JVCI*, 2016.
- [45] K. Takumi *et al.*, "Multispectral object detection for autonomous vehicles," in *ACM MM*, 2017.
- [46] Q. Ha *et al.*, "Mfnet: Towards real-time semantic segmentation for autonomous vehicles with multi-spectral scenes," in *IROS*, 2017.
- [47] FLIR, "Free teledyne flir thermal dataset for algorithm training," <https://www.flir.com/oem/adas/adas-dataset-form/>, 2018.
- [48] K. Song *et al.*, "Misaligned visible-thermal object detection: A drone-based benchmark and baseline," *TIV*, 2024.
- [49] J. Liu *et al.*, "Target-aware dual adversarial learning and a multi-scenario multi-modality benchmark to fuse infrared and visible for object detection," in *CVPR*, 2022.
- [50] R. I. Hammoud *et al.*, "Otcvbs benchmark dataset vollection," <http://vcip1-okstate.org/pbvs/bench/>, 2004.
- [51] A. Torabi *et al.*, "An iterative integrated framework for thermal-visible image registration, sensor fusion, and people tracking for video surveillance applications," *CVIU*, 2012.
- [52] C. Li *et al.*, "Learning collaborative sparse representation for grayscale-thermal tracking," *TIP*, 2016.
- [53] M. Kristan *et al.*, "The seventh visual object tracking vot2019 challenge results," in *ICCVW*, 2019.
- [54] Y. Zhang *et al.*, "Drone-based rgbt tiny person detection," *ISPRS*, 2023.
- [55] J. Wang *et al.*, "A normalized gaussian wasserstein distance for tiny object detection," *ISPRS*, 2022.
- [56] W. Liu *et al.*, "Ssd: Single shot multibox detector," in *ECCV*, 2016.
- [57] J. Redmon *et al.*, "You only look once: Unified, real-time object detection," in *CVPR*, 2016.
- [58] C. Feng *et al.*, "Tood: Task-aligned one-stage object detection," in *ICCV*, 2021.
- [59] S. Ren *et al.*, "Faster r-cnn: Towards real-time object detection with region proposal networks," *TPAMI*, 2017.
- [60] J. Wang *et al.*, "Side-aware boundary localization for more precise object detection," in *ECCV*, 2020.
- [61] Z. Cai *et al.*, "Cascade r-cnn: Delving into high quality object detection," in *CVPR*, 2018.
- [62] H. Zhang *et al.*, "Dynamic R-CNN: Towards high quality object detection via dynamic training," *ECCV*, 2020.
- [63] T.-Y. Lin *et al.*, "Focal loss for dense object detection," in *ICCV*, 2017.
- [64] X. Zhou *et al.*, "Objects as points," *ArXiv*, 2019.
- [65] Z. Tian *et al.*, "Fcos: Fully convolutional one-stage object detection," in *ICCV*, 2019.
- [66] S. Zhang *et al.*, "Bridging the gap between anchor-based and anchor-free detection via adaptive training sample selection," in *CVPR*, 2020.
- [67] H. Zhang *et al.*, "Varifocalnet: An iou-aware dense object detector," *CVPR*, 2021.
- [68] X. Zhu *et al.*, "Deformable detr: Deformable transformers for end-to-end object detection," in *ICLR*, 2020.
- [69] P. Sun *et al.*, "Sparse r-cnn: An end-to-end framework for object detection," *TPAMI*, 2023.
- [70] Z. Zong *et al.*, "Detrs with collaborative hybrid assignments training," in *ICCV*, 2023.
- [71] S. Chen *et al.*, "Diffusiondet: Diffusion model for object detection," in *ICCV*, 2023.
- [72] H. Zhang *et al.*, "Dino: Detr with improved denoising anchor boxes for end-to-end object detection," in *ICLR*, 2023.
- [73] S. Zhang *et al.*, "Dense distinct query for end-to-end object detection," in *CVPR*, 2023.
- [74] Y. Dai *et al.*, "Attentional local contrast networks for infrared small target detection," *TGRS*, 2021.
- [75] Y.-T. Chen *et al.*, "Multimodal object detection via probabilistic ensembling," in *ECCV*, 2022.
- [76] X. He *et al.*, "Multispectral object detection via cross-modal conflict-aware learning," in *ACM MM*, 2023.
- [77] Y. Kondo *et al.*, "MVA2023 Small Object Detection Challenge for Spotting Birds: Dataset, Methods, and Results," in *CVPR*, 2023.
- [78] Y. Dai *et al.*, "One-stage cascade refinement networks for infrared small target detection," *TGRS*, 2023.
- [79] H. Sun *et al.*, "Receptive-field and direction induced attention network for infrared dim small target detection with a large-scale dataset irdst," *TGRS*, 2023.
- [80] G. Chen *et al.*, "A survey of the four pillars for small object detection: Multiscale representation, contextual information, super-resolution, and region proposal," *TSMC*, 2022.
- [81] Y. Chen *et al.*, "Scale-aware automatic augmentation for object detection," in *CVPR*, 2021.
- [82] M. Kisantal *et al.*, "Augmentation for small object detection," *ArXiv*, 2019.
- [83] J. Han *et al.*, "Redet: A rotation-equivariant detector for aerial object detection," in *CVPR*, 2021.
- [84] T.-Y. Lin *et al.*, "Feature pyramid networks for object detection," in *CVPR*, 2017.
- [85] Y. Gong *et al.*, "Effective fusion factor in fpn for tiny object detection," in *WACV*, 2021.
- [86] B. Singh *et al.*, "Sniper: Efficient multi-scale training," *NeurIPS*, 2018.
- [87] S. Bell *et al.*, "Inside-outside net: Detecting objects in context with skip pooling and recurrent neural networks," in *CVPR*, 2016.
- [88] X. Tang *et al.*, "Pyramidbox: A context-assisted single shot face detector," in *ECCV*, 2018.
- [89] C. Deng *et al.*, "Extended feature pyramid network for small object detection," *TMM*, 2021.
- [90] P. Zhou *et al.*, "Scale-transferrable object detection," in *CVPR*, 2018.
- [91] J. Noh *et al.*, "Better to follow, follow to be better: Towards precise supervision of feature super-resolution for small object detection," in *ICCV*, 2019.
- [92] Y. Bai *et al.*, "Sod-mtgan: Small object detection via multi-task generative adversarial network," in *ECCV*, 2018.
- [93] J. Rivest *et al.*, "Detection of dim targets in digital infrared imagery by morphological image processing," *Opt. Eng.*, 1996.
- [94] Deshp *et al.*, "Max-mean and max-median filters for detection of small targets," in *SDPST*, 1999.
- [95] C. P. Chen *et al.*, "A local contrast method for small infrared target detection," *TGRS*, 2013.
- [96] J. Han *et al.*, "Infrared small target detection utilizing the multiscale relative local contrast measure," *GRSL*, 2018.
- [97] S. Moradi *et al.*, "A false-alarm aware methodology to develop robust and efficient multi-scale infrared small target detection algorithm," *Infrared Phys. Techn.*, 2018.
- [98] J. Han *et al.*, "Infrared small target detection based on the weighted strengthened local contrast measure," *GRSL*, 2020.
- [99] J. Han *et al.*, "A local contrast method for infrared small-target detection utilizing a tri-layer window," *GRSL*, 2019.
- [100] Y. Dai *et al.*, "Reweighted infrared patch-tensor model with both nonlocal and local priors for single-frame small target detection," *JSTAR*, 2017.

- [101] L. Zhang *et al.*, "Infrared small target detection via non-convex rank approximation minimization joint l2, 1 norm," *RS*, 2018.
- [102] T. Liu *et al.*, "Non-convex tensor low-rank approximation for infrared small target detection," *TGRS*, 2021.
- [103] L. Zhang *et al.*, "Infrared small target detection based on partial sum of the tensor nuclear norm," *RS*, 2019.
- [104] Y. Sun *et al.*, "Infrared dim and small target detection via multiple subspace learning and spatial-temporal patch-tensor model," *TGRS*, 2020.
- [105] M. Zhang *et al.*, "Rkformer: Runge-kutta transformer with random-connection attention for infrared small target detection," in *ACM MM*, 2022.
- [106] M. Zhang *et al.*, "Exploring feature compensation and cross-level correlation for infrared small target detection," in *TW ACM MM*, 2022.
- [107] M. Ju *et al.*, "Istdet: An efficient end-to-end neural network for infrared small target detection," *Infrared Phys. Techn.*, 2021.
- [108] Q. Hou *et al.*, "Ristdnet: Robust infrared small target detection network," *GRSL*, 2021.
- [109] D. Pang *et al.*, "Sttm-sfr: Spatial-temporal tensor modeling with saliency filter regularization for infrared small target detection," *TGRS*, 2022.
- [110] T. Liu *et al.*, "Nonconvex tensor low-rank approximation for infrared small target detection," *TGRS*, 2021.
- [111] Y. Zhang *et al.*, "Learning nonlocal quadrature contrast for detection and recognition of infrared rotary-wing uav targets in complex background," *TGRS*, 2022.
- [112] J. Du *et al.*, "A spatial-temporal feature-based detection framework for infrared dim small target," *TGRS*, 2021.
- [113] S. Hwang *et al.*, "Multispectral pedestrian detection: Benchmark dataset and baselines," in *CVPR*, 2015.
- [114] M. Yuan *et al.*, "Translation, scale and rotation: cross-modal alignment meets rgb-infrared vehicle detection," in *ECCV*, 2022.
- [115] Y.-T. Chen *et al.*, "Multimodal object detection via probabilistic ensembling," in *ECCV*, 2022.
- [116] H. Zhang *et al.*, "Multispectral fusion for object detection with cyclic fuse-and-refine blocks," in *ICIP*, 2020.
- [117] Y. Zhang *et al.*, "When pedestrian detection meets multimodal learning: Generalist model and benchmark dataset," in *ECCV*, 2024.
- [118] C. Li *et al.*, "Multispectral pedestrian detection via simultaneous detection and segmentation," in *BMVC*, 2018.
- [119] L. Zhang *et al.*, "Weakly aligned cross-modal learning for multispectral pedestrian detection," in *ICCV*, 2019.
- [120] J. U. Kim *et al.*, "Towards versatile pedestrian detector with multisensory-matching and multispectral recalling memory," in *AAAI*, 2022.
- [121] C. Chen *et al.*, "Weakly misalignment-free adaptive feature alignment for uavs-based multimodal object detection," in *CVPR*, 2024.
- [122] D. Guan *et al.*, "Fusion of multispectral data through illumination-aware deep neural networks for pedestrian detection," *IF*, 2019.
- [123] Y. Zhang *et al.*, "Illumination-guided rgbt object detection with inter-and intra-modality fusion," *TIM*, 2023.
- [124] Q. Xu *et al.*, "Heterogeneous graph transformer for multiple tiny object tracking in rgb-t videos," *TMM*, 2024.
- [125] H. Rezatofghi *et al.*, "Generalized intersection over union: A metric and a loss for bounding box regression," in *CVPR*, 2019.
- [126] Z. Zheng *et al.*, "Distance-iou loss: Faster and better learning for bounding box regression," in *AAAI*, 2020.
- [127] Z. Zhang, "Flexible camera calibration by viewing a plane from unknown orientations," in *ICCV*, 1999.
- [128] Z. Zhang, "A flexible new technique for camera calibration," *TPAMI*, 2000.
- [129] L. Wang *et al.*, "Parallax attention for unsupervised stereo correspondence learning," *TPAMI*, 2020.
- [130] D. Programmer, "Darklabel," <http://darkpgmr.tistory.com/16>, 2022.
- [131] H. Xie *et al.*, "Prcl: Probabilistic representation contrastive learning for semi-supervised semantic segmentation," *IJCV*, 2024.
- [132] K. Chen *et al.*, "MMDetection: Open mmlab detection toolbox and benchmark," *ArXiv*, 2019.
- [133] K. He *et al.*, "Deep residual learning for image recognition," in *CVPR*, 2016.
- [134] Y. Xinyi *et al.*, "Basicirstd," <https://github.com/XinyiYing/BasicIRSTD>, 2021.
- [135] P. Sun *et al.*, "Sparse r-cnn: End-to-end object detection with learnable proposals," in *CVPR*, 2021.

# Visible-Thermal Tiny Object Detection: A Benchmark Dataset and Baselines

## (Supplemental Material)

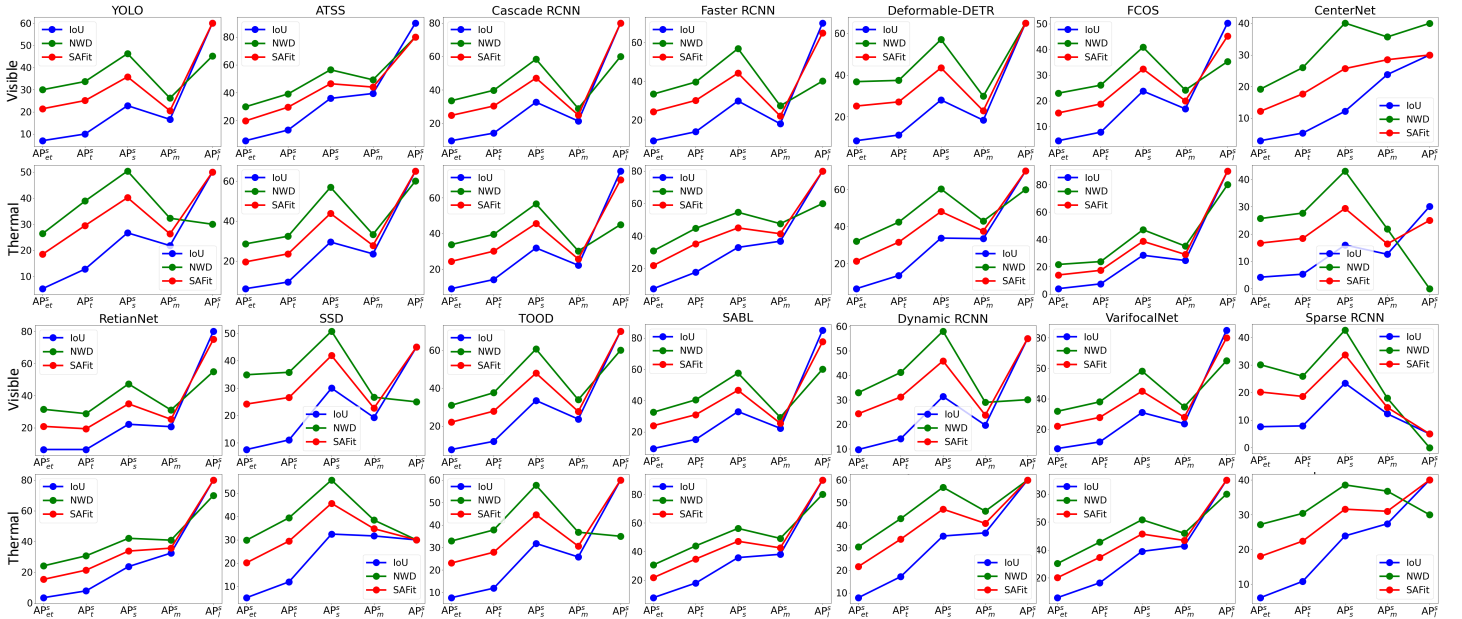


Fig. I: Comparisons among different measures for performance evaluation in visible and thermal modalities under  $C=32$ .  $AP_{et}^s$ ,  $AP_t^s$ ,  $AP_s^s$ ,  $AP_m^s$ ,  $AP_l^s$  represent AP values of extremely tiny, tiny, small, medium, large targets.

First, we provide more evaluation results of SAFit measure for the analyses in Section 4.1-SAFit Measure for Evaluation. Second, we provide more SAFit-based and IoU-based results of SAFit loss in RGBT-Tiny datasets for the analyses in Section 4.1-SAFit Loss for Training. Fourth, we provide IoU-based results of RGBT-Tiny benchmark for the analyses in Section 4.2. Finally, we make discussions on some typical failure cases of existing state-of-the-art algorithms and provide some potential solutions.

### A RESULTS OF SAFIT MEASURE FOR EVALUATION

We employ IoU, NWD and SAFit measures under different  $C$  values (*i.e.*,  $C=16$ ,  $C=32$ ) for performance evaluation on 14 recent state-of-the-art visible generic detection methods [56–69]. AP results in visible and thermal modalities across different target scales (*i.e.*, extremely tiny, tiny, small, medium, large) are shown in Figs. I and II. It can be observed that AP values of SAFit are closer to those of NWD when GT bbox size is smaller, and approximate those of IoU as size increases. In addition,  $C$  controls the maximum values of NWD and SAFit, and a higher  $C$  value results in higher NWD and SAFit values. Moreover,  $C$  controls the transition point of dominated measures. That is, when GT bbox size is smaller than  $C$ , NWD occupies more proportions of SAFit, while a larger GT bbox size results in IoU domination. In conclusion, extensive

experimental results have demonstrated that SAFit can make comprehensively reasonable evaluations on both large and small targets, and can flexibly control the transition point by a size-aware parameter  $C$  for custom requirements.

### B RESULTS OF SAFIT LOSS FOR TRAINING

Tables I and II provide SAFit-based and IoU-based results achieved by different detectors (*i.e.*, ATSS [66], Sparse RCNN [69]) with different losses (*i.e.*, IoU [80], DIOU [126], CIOU [126], GIoU [125], NWD [55] and SAFit losses) in visible modality of RGBT-Tiny dataset. Note that, we employ 2 variants of SAFit loss (*i.e.*, SAFit-s and SAFit<sub>g</sub>) to investigate the performance of direct transition (*i.e.*, loss function is set to NWD when GT box size is smaller than  $C$ , while set to IoU vice versa) and stronger component (*i.e.*, Sigmoid weighted combination of GIoU and NWD). It can be observed that SAFit loss shows high robustness to different detectors under both IoU and SAFit metrics. In addition, compared with SAFit-s loss, SAFit loss achieves higher AP values, which demonstrates that size-aware weighted summation is superior to direct transition. Moreover, SAFit<sub>g</sub> performs superior to SAFit, which demonstrates that stronger components further promote the detection performance. Furthermore, compared with its components, SAFit<sub>g</sub> and SAFit achieves higher  $AP_{et}^s$ ,  $AP_t^s$  values than NWD, and higher  $AP_m^s$  values than GIoU

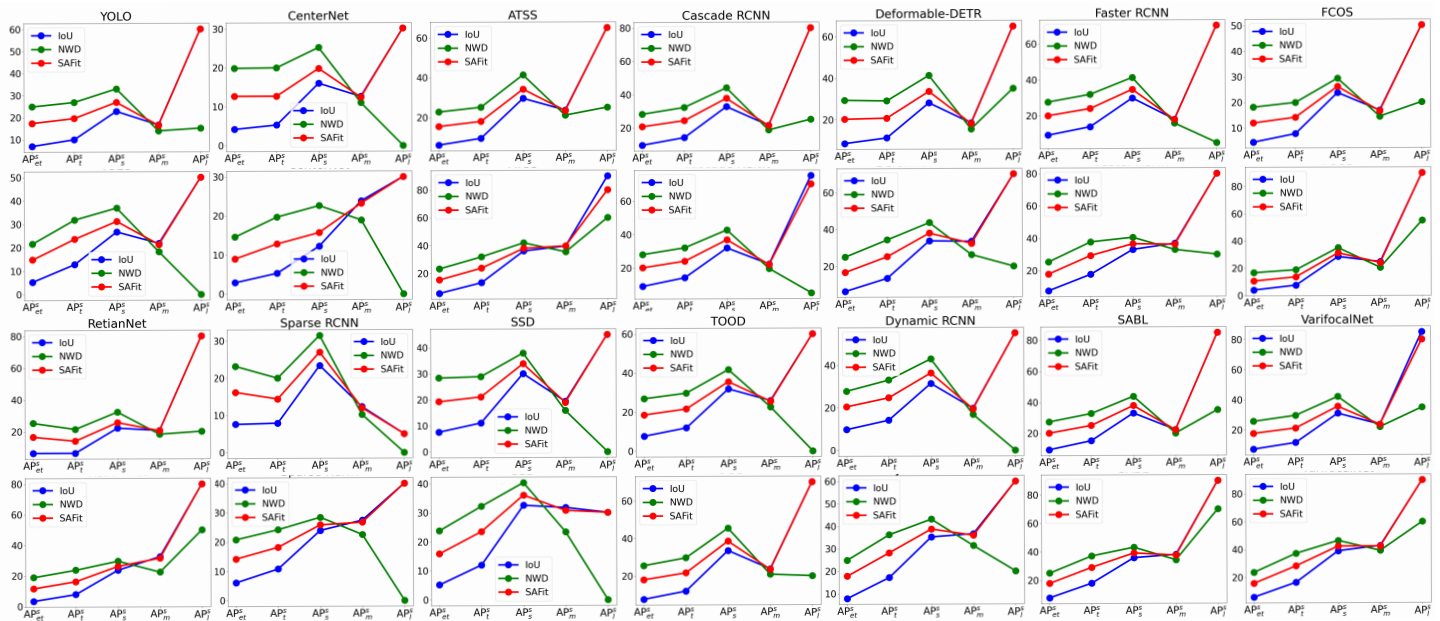


Fig. II: Comparisons among different measures for performance evaluation in visible and thermal modalities under  $C=16$ .  $AP_{et}^s$ ,  $AP_t^s$ ,  $AP_s^s$ ,  $AP_m^s$ ,  $AP_l^s$  represent AP values of extremely tiny, tiny, small, medium, large targets.

TABLE I: SAFit-based results of different losses equipped with different detectors. SAFit-s, SAFit<sub>g</sub> are used to investigate the effect of direct transition (*i.e.*, loss function is set to NWD when GT box size is smaller than  $C$ , while set to IoU vice versa) and stronger components (*i.e.*, Sigmoid weighted summation of Giou and NWD). Best results are shown in boldface, and second best results are underlined.

Loss	ATSS									Sparse RCNN								
	AP	AP <sub>50</sub>	AP <sub>75</sub>	AP <sub>et</sub> <sup>s</sup>	AP <sub>t</sub> <sup>s</sup>	AP <sub>s</sub> <sup>s</sup>	AP <sub>m</sub> <sup>s</sup>	AP <sub>l</sub> <sup>s</sup>	AR	AP	AP <sub>50</sub>	AP <sub>75</sub>	AP <sub>et</sub> <sup>s</sup>	AP <sub>t</sub> <sup>s</sup>	AP <sub>s</sub> <sup>s</sup>	AP <sub>m</sub> <sup>s</sup>	AP <sub>l</sub> <sup>s</sup>	AR
GIoU	24.2	38.1	<u>26.8</u>	19.6	23.6	43.8	27.5	65.0	<u>38.0</u>	19.2	29.8	21.9	18.8	<u>19.5</u>	33.4	14.9	40.1	33.7
DIoU	23.6	37.5	26.1	19.2	23.1	43.6	<u>28.2</u>	<b>80.0</b>	36.8	19.1	29.7	21.7	19.7	18.5	33.9	14.7	<u>60.1</u>	33.7
CIoU	24.2	39.1	26.0	19.6	24.2	42.6	<b>29.0</b>	65.0	37.4	20.0	30.6	23.0	19.5	19.0	33.9	14.8	<b>80.1</b>	33.9
IoU	23.3	37.3	24.9	19.3	23.7	42.3	26.5	<u>75.0</u>	37.4	8.1	14.7	8.5	11.3	7.1	11.8	0.2	0.0	24.1
NWD	24.1	38.6	26.2	19.6	23.6	<u>44.2</u>	27.0	60.0	<b>38.4</b>	19.7	30.2	23.2	19.7	18.4	<u>35.8</u>	<u>15.2</u>	50.0	34.0
SAFit-s	24.3	39.0	26.2	<u>19.7</u>	24.3	42.1	27.5	60.0	36.8	19.8	31.2	22.5	18.4	19.4	35.5	14.5	50.1	34.2
SAFit	<u>24.5</u>	<u>39.2</u>	26.6	<u>19.7</u>	<b>25.1</b>	43.5	28.0	60.1	37.4	<u>21.4</u>	<u>32.2</u>	<u>25.0</u>	<u>20.4</u>	<b>20.5</b>	<b>36.3</b>	14.5	15.0	<b>35.8</b>
SAFit <sub>g</sub>	<b>24.7</b>	<b>39.3</b>	27.1	<b>20.6</b>	23.6	<b>44.4</b>	27.5	70.0	37.4	<b>22.0</b>	<b>34.0</b>	<b>25.2</b>	<b>22.2</b>	<u>19.5</u>	34.9	<b>16.3</b>	15.0	<u>34.5</u>

and IoU respectively, which demonstrates that our size-aware weighted summation can not only combine both advantages of its components but also produce a breakthrough by offering a more stable and smooth training for targets with varied sizes.

### C IoU-BASED RESULTS OF RGBT-TINY BENCHMARK

Table III provides IoU-based results of our benchmark. It can be observed that IoU-based results are lower than SAFit-based results, and the differences result from unreasonable performance evaluation of IoU-based metrics on small objects.

### D TYPICAL FAILURE CASES AND POTENTIAL SOLUTIONS

Figure III visualizes some typical failure cases of existing state-of-the-art algorithms. Detailed discussions are as follows with some potential solutions being provided.

- 1) **Extremely tiny object size:** As shown in Fig. III (a), the extremely small object size with significantly

fewer appearance cues raises serious limitations for feature representation learning, and thus results in high miss detection and false alarm. This limitation highlights the need for exploring multi-dimensional reliable information (*e.g.*, appearance, context, motion, radiation information) for object detection.

- 2) **Spatio-Temporal Misalignment:** As shown in Fig. III (b), the inherent disparity variation of dual lenses [129] presents significant challenges in RGBT fusion, and thus leads to suboptimal detection performance. This limitation highlights the need for dynamic cross-modal feature alignment.
- 3) **Low Light Vision:** As shown in Fig. III (c), extreme asymmetric visible and thermal information of low light vision (*e.g.*, low and invisible light vision) introduce difficulties in RGBT fusion, resulting in detection performance degradation. This limitation highlights the need for illumination-aware cross-modal feature compensation.

TABLE II: IoU-based results of different losses equipped with different detectors. SAFit-s, SAFit<sub>g</sub> are used to investigate the effect of direct transition (*i.e.*, loss function is set to NWD when GT box size is smaller than  $C$ , while set to IoU vice versa) and stronger components (*i.e.*, Sigmoid weighted summation of GIoU and NWD). Best results are shown in boldface, and second best results are underlined.

Loss	ATSS									Sparse RCNN								
	AP	AP <sub>50</sub>	AP <sub>75</sub>	AP <sub>et</sub> <sup>s</sup>	AP <sub>t</sub> <sup>s</sup>	AP <sub>s</sub> <sup>s</sup>	AP <sub>m</sub> <sup>s</sup>	AP <sub>l</sub> <sup>s</sup>	AR	AP	AP <sub>50</sub>	AP <sub>75</sub>	AP <sub>et</sub> <sup>s</sup>	AP <sub>t</sub> <sup>s</sup>	AP <sub>s</sub> <sup>s</sup>	AP <sub>m</sub> <sup>s</sup>	AP <sub>l</sub> <sup>s</sup>	AR
GIoU	10.9	25.3	8.1	6.1	<u>9.5</u>	28.6	22.3	60.0	<u>19.1</u>	9.1	21.4	<u>6.4</u>	7.3	<b>9.0</b>	23.3	<u>12.6</u>	45.0	19.2
DIoU	10.9	25.6	8.0	6.0	8.9	28.6	<u>24.1</u>	<b>80.0</b>	18.9	8.9	20.9	6.2	7.4	8.1	23.3	12.3	<u>60.1</u>	18.9
CIoU	11.0	25.9	<b>8.3</b>	<b>6.3</b>	9.0	28.3	<b>24.9</b>	65.0	<u>19.1</u>	9.6	22.7	<b>6.5</b>	7.8	<u>8.8</u>	23.4	12.3	<b>80.1</b>	<u>19.8</u>
IoU	10.6	25.0	8.0	5.8	9.2	28.2	22.2	<u>75.0</u>	19.0	2.6	7.8	0.9	3.2	2.4	6.5	0.1	0.0	11.9
NWD	10.7	25.8	7.7	5.9	9.0	<u>29.8</u>	22.7	60.0	19.2	8.6	22.0	4.6	7.2	8.1	22.8	12.5	55.0	18.5
SAFit-s	10.6	<u>26.0</u>	7.5	6.1	8.8	27.9	22.8	60.0	18.2	8.4	21.4	4.9	6.3	8.0	22.6	11.5	50.1	18.6
SAFit	<u>11.2</u>	<b>26.9</b>	<u>8.1</u>	<u>6.2</u>	<b>9.6</b>	28.6	23.4	60.1	19.0	<u>10.0</u>	<u>23.9</u>	<u>6.4</u>	<u>8.3</u>	<b>9.0</b>	<b>25.0</b>	11.9	20.0	<b>20.4</b>
SAFit <sub>g</sub>	<b>11.4</b>	<b>26.9</b>	<b>8.3</b>	<b>6.3</b>	9.3	<b>30.2</b>	23.1	70.0	19.1	<b>10.1</b>	<b>24.4</b>	<b>6.5</b>	<b>8.7</b>	<u>8.8</u>	<u>23.5</u>	<b>13.3</b>	15.0	19.5

TABLE III: IoU-based results of existing visible generic detection (V-D), visible SOD (V-SOD), thermal SOD (T-SOD), RGBT detection methods (RGBT-D) methods on RGBT-Tiny dataset. “#Param.” represents the number of parameters. AP<sub>et</sub><sup>s</sup>, AP<sub>t</sub><sup>s</sup>, AP<sub>s</sub><sup>s</sup>, AP<sub>m</sub><sup>s</sup>, AP<sub>l</sub><sup>s</sup> represent AP values of extremely tiny, tiny, small, medium, large targets. “(-)” represents network trained under replicated visible or thermal inputs to investigate the influence of multimodal fusion. Note that, the results of T-SOD are trained with hard (left) and soft (right) masks generated by bboxes under uniform and Gaussian distributions.

	Methods	#Param.	Visible									Thermal								
			AP	AP <sub>50</sub>	AP <sub>75</sub>	AP <sub>et</sub> <sup>s</sup>	AP <sub>t</sub> <sup>s</sup>	AP <sub>s</sub> <sup>s</sup>	AP <sub>m</sub> <sup>s</sup>	AP <sub>l</sub> <sup>s</sup>	AR	AP	AP <sub>50</sub>	AP <sub>75</sub>	AP <sub>et</sub> <sup>s</sup>	AP <sub>t</sub> <sup>s</sup>	AP <sub>s</sub> <sup>s</sup>	AP <sub>m</sub> <sup>s</sup>	AP <sub>l</sub> <sup>s</sup>	AR
V-D	SSD [56]	25.2M	12.6	31.0	8.6	7.6	11.1	30.0	19.3	45.0	19.1	12.2	30.4	7.5	5.2	12.0	32.5	31.7	30.0	18.9
	YOLO [57]	61.5M	10.0	26.7	5.1	7.0	10.0	22.8	16.6	60.1	15.9	10.6	27.8	6.0	5.3	12.8	26.7	21.8	50.0	17.1
	TOOD [58]	31.8M	13.0	30.3	9.9	7.7	11.9	31.8	25.8	60.0	20.2	13.4	31.1	10.3	7.7	12.0	33.5	23.7	70.0	20.7
	ATSS [66]	31.9M	10.9	25.3	8.1	6.1	9.5	28.6	22.3	60.0	19.1	13.8	32.0	9.6	5.7	13.3	36.0	39.5	<u>90.0</u>	21.7
	RetinaNet [63]	36.2M	8.1	21.7	4.5	6.5	6.5	22.2	20.7	80.1	16.5	7.9	20.3	5.1	3.5	7.9	23.7	32.5	80.0	17.8
	Faster RCNN [59]	41.2M	14.1	32.5	10.0	9.3	13.9	29.8	18.0	70.1	19.9	15.4	35.2	10.5	7.6	17.7	33.0	36.8	80.0	21.1
	Cascade RCNN [61]	68.9M	15.0	33.9	11.1	9.7	14.2	32.7	21.4	80.0	20.5	14.6	32.8	11.2	9.1	14.2	31.9	22.2	75.0	19.6
	Dynamic RCNN [62]	41.2M	14.5	33.5	10.7	9.8	14.2	31.4	19.7	55.0	20.2	15.2	33.7	11.3	7.9	17.2	35.2	36.6	60.0	20.9
	SABL [60]	41.9M	15.1	33.6	11.9	9.4	15.2	33.0	22.3	85.0	20.3	15.8	34.6	12.4	7.8	18.0	35.8	38.1	<u>90.0</u>	21.5
	CenterNet [64]	14.4M	5.6	17.3	2.0	4.2	5.3	16.0	12.6	30.1	11.6	5.3	16.1	1.8	2.9	5.3	12.2	23.8	30.0	12.2
	FCOS [65]	31.9M	7.6	18.5	5.3	4.5	7.8	23.8	16.9	50.3	14.4	8.2	19.2	5.7	4.0	7.5	28.4	24.6	<u>90.0</u>	15.8
	VarifocalNet [67]	32.5M	13.0	29.4	10.1	7.4	11.7	31.0	23.7	85.0	20.3	15.9	35.3	12.0	5.9	16.5	39.0	42.8	<u>90.0</u>	22.9
	Deformable DETR [68]	39.8M	12.3	30.9	7.3	8.6	11.3	28.1	18.4	65.0	20.5	13.0	33.1	7.6	6.5	13.6	33.8	33.5	70.0	21.3
	Sparse RCNN [69]	44.2M	9.1	21.4	6.4	7.3	9.0	23.3	12.6	45.0	19.2	10.3	23.4	7.8	6.1	10.8	23.9	27.4	40.0	22.0
	CO-DETR [70]	65.2M	<u>17.8</u>	39.1	<u>14.6</u>	<u>11.8</u>	17.5	34.4	<u>30.6</u>	<u>90.0</u>	27.2	<u>19.6</u>	<u>40.9</u>	<b>16.6</b>	<u>9.2</u>	<u>21.9</u>	<u>40.4</u>	<b>45.0</b>	<b>100.0</b>	29.8
	DiffusionDet [71]	151.0M	<b>19.7</b>	<b>42.4</b>	<b>16.2</b>	<b>13.6</b>	<u>18.5</u>	<u>39.9</u>	27.0	85.0	<u>28.5</u>	<b>19.7</b>	<b>41.8</b>	<b>16.6</b>	<u>11.4</u>	<u>20.4</u>	<b>45.5</b>	<u>42.3</u>	<u>90.0</u>	29.7
DINO [72]	97.7M	17.0	39.6	11.7	9.5	<b>18.7</b>	<b>40.4</b>	<b>40.8</b>	<u>90.0</u>	<b>30.0</b>	17.1	39.0	12.3	8.3	18.5	39.9	40.2	<u>90.0</u>	28.7	
DDQ [73]	48.3M	15.2	34.6	11.7	9.3	14.5	34.1	29.5	85.0	26.2	18.9	39.8	<u>15.5</u>	9.6	19.5	42.6	41.8	<u>90.0</u>	30.6	
V-SOD	QueryDet [13]	39.4M	10.8	27.4	6.5	5.9	10.8	25.5	16.1	35.0	7.6	11.5	29.8	5.8	4.6	13.8	27.9	17.8	40.0	8.3
	RFLA [12]	36.3M	14.3	34.0	9.7	9.5	14.0	31.2	25.0	50.0	23.0	16.4	38.1	11.4	8.8	18.7	35.9	34.4	60.0	25.6
	C3Det [14]	55.3M	6.3	12.2	5.7	0.0	4.0	29.2	21.6	81.7	3.7	7.8	14.6	7.8	0.1	4.1	33.8	40.8	80.0	5.2
T-SOD	ACM [27]	<b>0.4M</b>	0.0	0.0	0.0	0.0	0.0	0.0	0.0	0.0	0.0	6.9	17.2	4.2	3.8	6.7	16.6	23.5	65.0	10.2
	ALCNet [74]	<b>0.4M</b>	0.0	0.0	0.0	0.0	0.0	0.1	0.0	0.0	0.2	3.6	7.5	3.3	0.4	2.8	8.5	19.0	60.0	4.5
	DNA-Net [24]	<u>4.7M</u>	0.5	1.5	0.2	0.0	0.9	1.8	9.3	0.0	2.8	2.0	5.7	1.0	1.1	1.5	8.7	3.5	0.0	3.8
RGBT-D	UA-CMDet (-) [36]	139.2M	8.6	21.2	5.5	3.2	9.1	27.5	17.0	52.1	5.7	11.9	29.4	7.1	3.4	11.9	31.6	38.4	32.5	8.5
	UA-CMDet [36]	139.2M	6.1	16.7	3.2	2.2	5.7	19.3	12.3	20.1	5.4	8.0	21.0	4.4	1.8	7.5	18.8	34.8	13.1	5.8
	ProbEn-early [75]	60.3M	3.2	8.7	1.6	1.1	4.3	5.9	12.4	0.0	0.7	7.4	18.9	4.2	3.6	8.3	21.6	18.8	76.7	5.5
	ProbEn-middle (-) [75]	120.6M	12.8	29.2	9.1	8.6	12.0	28.5	23.9	85.0	8.6	14.1	31.3	10.1	7.0	16.4	30.6	32.5	85.0	8.5
	ProbEn-middle [75]	120.6M	13.3	32.0	8.3	9.0	13.1	27.3	27.5	<b>92.5</b>	19.2	15.5	34.6	11.3	8.6	17.2	34.0	34.3	70.0	10.1
	QFDet [54]	60.3M	13.6	36.0	7.7	8.8	13.6	30.6	20.6	72.5	22.1	16.6	38.9	11.2	<b>13.0</b>	18.1	21.3	20.0	50.0	<b>31.2</b>
	CALNet [76]	153.6M	10.6	29.2	5.0	8.1	12.6	23.0	6.8	10.0	16.9	12.7	33.1	7.0	8.0	15.7	28.4	20.1	5.4	18.6
CMA-Det [48]	33.4M	5.5	16.1	2.2	3.3	5.7	15.2	9.1	54.7	13.0	5.6	16.9	2.5	3.1	6.2	8.0	21.5	70.0	12.6	

- Inter-class Homogeneity:** As shown in Fig. III (d), similar feature representation across classes results in semantic ambiguity, over-fitting in training data and ambiguous decision logic, and thus leads to limited recognition performance, poor interpretability and inferior generalization. This limitation highlights the need to explore more discriminative features (*e.g.*, appearance, context, motion, radiation information and multi-dimensional combination) for object recognition.
- Intra-class Variations:** As shown in Fig. III (e), object appearance can be significantly changed due to

complex object states (*e.g.*, shape, texture, color and posture) and observation states (distance, orientation, light, weather, sensor motion, sensor noise), resulting in miss detection and false alarms. This limitation highlights the need for long-term temporal information exploration to assist object detection and recognition.

- Severe occlusion:** As shown in Fig. III (f), algorithms often struggle to accurately identify and localize the object of interest when partially or completely occluded, resulting in a significant drop in detection rates. This limitation highlights the need for occlusion

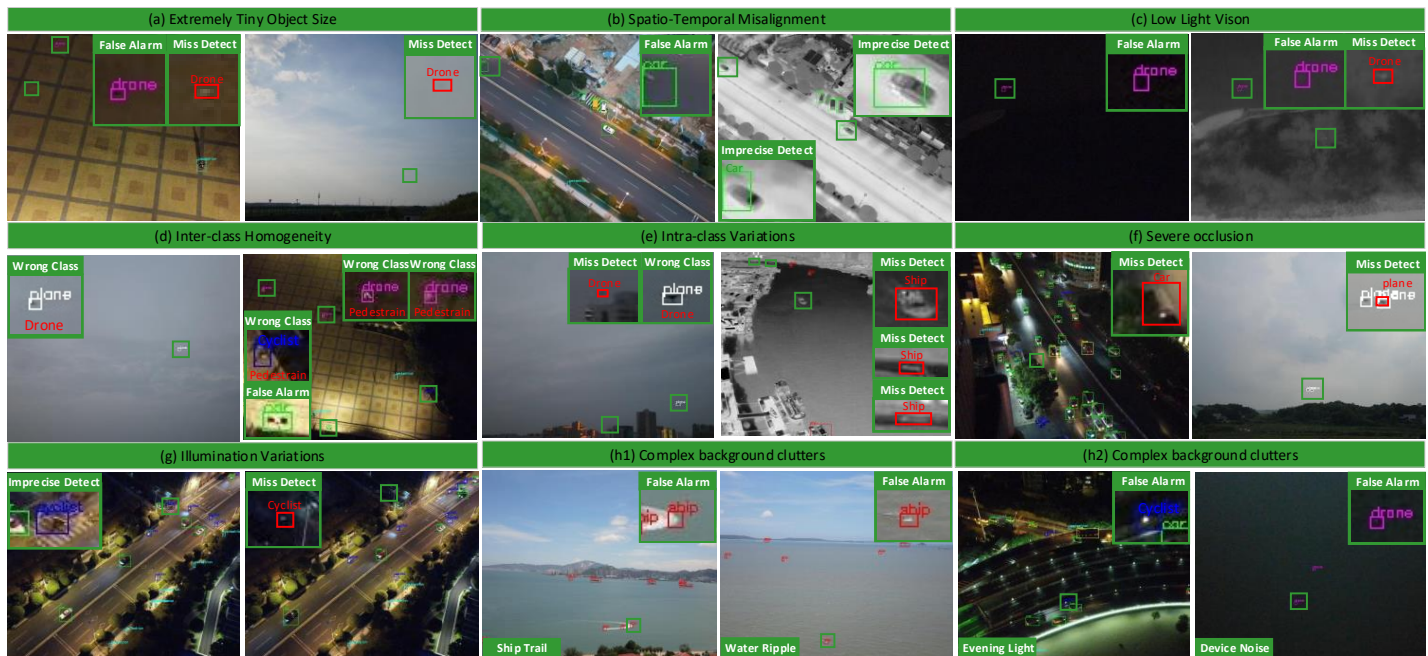


Fig. III: Failure cases of existing state-of-the-art algorithms. Green boxes show the zoom-in target regions. Red boxes & texts inside represent GT boxes and classes.

context reasoning, including leveraging generative models to infer the shape and appearance of occluded objects, and incorporating physical and geometric constraints to predict the likelihood of occlusion. In addition, the interaction or occlusion of densely arranged objects often leads to performance drop. This limitation highlights the need for effective disentangling techniques (such as image super-resolution techniques to integrate spatial prior knowledge and graph-based representations for object reconstruction), and temporal consecutive reasoning.

- 7) **Illumination Variations:** As shown in Fig. III (g), Illumination variations, particularly in night-time scenarios, pose significant challenges in object detection and recognition systems. This limitation highlights the need for image enhancement and multimodal fusion to improve the robustness.
- 8) **Complex background clutters:** As shown in Figs. III (h1), (h2), complex background clutters (e.g., ship trail, water ripple, evening lights and device noise) significantly affect the detection of small objects, resulting in high false alarms. This limitation highlights the need for more robust and adaptive algorithms that can effectively cope with the complexities and diversities of real-world imagery.

## REFERENCES

- [1] T.-Y. Lin *et al.*, "Microsoft coco: Common objects in context," in *ECCV*, 2014.
- [2] P. Zhu *et al.*, "Detection and tracking meet drones challenge," *TPAMI*, 2021.
- [3] Zhao, Jian *et al.*, "Towards pose invariant face recognition in the wild," in *CVPR*, 2018.
- [4] Zhao, Jian *et al.*, "3d-aided dual-agent gans for unconstrained face recognition," *TPAMI*, 2018.
- [5] Y. Pang *et al.*, "Tju-dhd: A diverse high-resolution dataset for object detection," *TIP*, 2020.
- [6] Zhao, Jian *et al.*, "Dual-agent gans for photorealistic and identity preserving profile face synthesis," *NeurIPS*, 2017.
- [7] Zhao, Jian *et al.*, "Look across elapse: Disentangled representation learning and photorealistic cross-age face synthesis for age-invariant face recognition," *AAAI*, 2019.
- [8] G. Cheng *et al.*, "Towards large-scale small object detection: Survey and benchmarks," *TPAMI*, 2023.
- [9] Zhao, Jian *et al.*, "Towards age-invariant face recognition," *TPAMI*, 2020.
- [10] Zhao, Jian *et al.*, "3d-aided deep pose-invariant face recognition," in *IJCAI*, 2018.
- [11] Q. Wang *et al.*, "Face.evolve: A cross-platform library for high-performance face analytics," *Neurocomputing*, 2022.
- [12] C. Xu *et al.*, "Rfla: Gaussian receptive based label assignment for tiny object detection," in *ECCV*, 2022.
- [13] C. Yang *et al.*, "Querydet: Cascaded sparse query for accelerating high-resolution small object detection," in *CVPR*, 2022.
- [14] C. Lee *et al.*, "Interactive multi-class tiny-object detection," in *CVPR*, 2022.
- [15] F. C. Akyon *et al.*, "Slicing aided hyper inference and fine-tuning for small object detection," *ICIP*, 2022.
- [16] S. Zhang *et al.*, "Widerperson: A diverse dataset for dense pedestrian detection in the wild," *TMM*, 2019.
- [17] J. Ding *et al.*, "Object detection in aerial images: A large-scale benchmark and challenges," *TPAMI*, 2021.
- [18] C. Chen *et al.*, "R-cnn for small object detection," in *ACCV*, 2017.
- [19] X. Yu *et al.*, "Scale match for tiny person detection," in *WACV*, 2020.
- [20] S. Yang *et al.*, "Wider face: A face detection benchmark," in *CVPR*, 2016.
- [21] M. Braun *et al.*, "Eurocity persons: A novel benchmark for

- person detection in traffic scenes," *TPAMI*, 2019.
- [22] J. Han *et al.*, "Soda10m: A large-scale 2d self/semi-supervised object detection dataset for autonomous driving," *NeurIPS*, 2021.
- [23] M. Zhang *et al.*, "Isnet: Shape matters for infrared small target detection," in *CVPR*, 2022.
- [24] B. Li *et al.*, "Dense nested attention network for infrared small target detection," *TIP*, 2022.
- [25] H. Wang *et al.*, "Miss detection vs. false alarm: Adversarial learning for small object segmentation in infrared images," in *ICCV*, 2019.
- [26] C. Gao *et al.*, "Infrared patch-image model for small target detection in a single image," *TIP*, 2013.
- [27] Y. Dai *et al.*, "Asymmetric contextual modulation for infrared small target detection," in *WACV*, 2021.
- [28] T. Wu *et al.*, "Mtu-net: Multi-level transunet for space-based infrared tiny ship detection," *ArXiv*, 2022.
- [29] X. Sun *et al.*, "A dataset for small infrared moving target detection under clutter background," *CSD*, 2021.
- [30] B. Hui *et al.*, "A dataset for infrared detection and tracking of dim-small aircraft targets under ground / air background," *CSD*, 2020.
- [31] M. Zhao *et al.*, "Tbc-net: A real-time detector for infrared small target detection using semantic constraint," *ArXiv*, 2019.
- [32] N. Jiang *et al.*, "Anti-uav: a large-scale benchmark for vision-based uav tracking," *TMM*, 2021.
- [33] R. Fu *et al.*, "A dataset for infrared time-sensitive target detection and tracking for air-ground application," *CSD*, 2022.
- [34] S. Hwang *et al.*, "Multispectral pedestrian detection: Benchmark dataset and baseline," in *CVPR*, 2015.
- [35] K. Zhou *et al.*, "Improving multispectral pedestrian detection by addressing modality imbalance problems," in *ECCV*, 2020.
- [36] Y. Sun *et al.*, "Drone-based rgb-infrared cross-modality vehicle detection via uncertainty-aware learning," *TCSVT*, 2022.
- [37] B. Huang *et al.*, "Anti-uav410: A thermal infrared benchmark and customized scheme for tracking drones in the wild," *TPAMI*, 2023.
- [38] C. Li *et al.*, "Lasher: A large-scale high-diversity benchmark for rgbt tracking," *TIP*, 2021.
- [39] C. Li *et al.*, "Weighted sparse representation regularized graph learning for rgb-t object tracking," in *ACM MM*, 2017.
- [40] C. Li *et al.*, "Rgb-t object tracking: Benchmark and baseline," *PR*, 2019.
- [41] P. Zhang *et al.*, "Visible-thermal uav tracking: A large-scale benchmark and new baseline," in *CVPR*, 2022.
- [42] A. González *et al.*, "Pedestrian detection at day/night time with visible and fir cameras: A comparison," *Sensors*, 2016.
- [43] X. Jia *et al.*, "Llvip: A visible-infrared paired dataset for low-light vision," in *ICCV*, 2021.
- [44] S. Razakarivony *et al.*, "Vehicle detection in aerial imagery: A small target detection benchmark," *JVCI*, 2016.
- [45] K. Takumi *et al.*, "Multispectral object detection for autonomous vehicles," in *ACM MM*, 2017.
- [46] Q. Ha *et al.*, "Mfnet: Towards real-time semantic segmentation for autonomous vehicles with multi-spectral scenes," in *IROS*, 2017.
- [47] FLIR, "Free teledyne flir thermal dataset for algorithm training," <https://www.flir.com/oem/adas/adas-dataset-form/>, 2018.
- [48] K. Song *et al.*, "Misaligned visible-thermal object detection: A drone-based benchmark and baseline," *TIV*, 2024.
- [49] J. Liu *et al.*, "Target-aware dual adversarial learning and a multi-scenario multi-modality benchmark to fuse infrared and visible for object detection," in *CVPR*, 2022.
- [50] R. I. Hammoud *et al.*, "Otcbsv benchmark dataset collection," <http://vcip1-okstate.org/pbvs/bench/>, 2004.
- [51] A. Torabi *et al.*, "An iterative integrated framework for thermal-visible image registration, sensor fusion, and people tracking for video surveillance applications," *CVIU*, 2012.
- [52] C. Li *et al.*, "Learning collaborative sparse representation for grayscale-thermal tracking," *TIP*, 2016.
- [53] M. Kristan *et al.*, "The seventh visual object tracking vot2019 challenge results," in *ICCVW*, 2019.
- [54] Y. Zhang *et al.*, "Drone-based rgbt tiny person detection," *ISPRS*, 2023.
- [55] J. Wang *et al.*, "A normalized gaussian wasserstein distance for tiny object detection," *ISPRS*, 2022.
- [56] W. Liu *et al.*, "Ssd: Single shot multibox detector," in *ECCV*, 2016.
- [57] J. Redmon *et al.*, "You only look once: Unified, real-time object detection," in *CVPR*, 2016.
- [58] C. Feng *et al.*, "Tood: Task-aligned one-stage object detection," in *ICCV*, 2021.
- [59] S. Ren *et al.*, "Faster r-cnn: Towards real-time object detection with region proposal networks," *TPAMI*, 2017.
- [60] J. Wang *et al.*, "Side-aware boundary localization for more precise object detection," in *ECCV*, 2020.
- [61] Z. Cai *et al.*, "Cascade r-cnn: Delving into high quality object detection," in *CVPR*, 2018.
- [62] H. Zhang *et al.*, "Dynamic R-CNN: Towards high quality object detection via dynamic training," *ECCV*, 2020.
- [63] T.-Y. Lin *et al.*, "Focal loss for dense object detection," in *ICCV*, 2017.
- [64] X. Zhou *et al.*, "Objects as points," *ArXiv*, 2019.
- [65] Z. Tian *et al.*, "Fcos: Fully convolutional one-stage object detection," in *ICCV*, 2019.
- [66] S. Zhang *et al.*, "Bridging the gap between anchor-based and anchor-free detection via adaptive training sample selection," in *CVPR*, 2020.
- [67] H. Zhang *et al.*, "Varifocalnet: An iou-aware dense object detector," *CVPR*, 2021.
- [68] X. Zhu *et al.*, "Deformable detr: Deformable transformers for end-to-end object detection," in *ICLR*, 2020.
- [69] P. Sun *et al.*, "Sparse r-cnn: An end-to-end framework for object detection," *TPAMI*, 2023.
- [70] Z. Zong *et al.*, "Detrs with collaborative hybrid assignments training," in *ICCV*, 2023.
- [71] S. Chen *et al.*, "Diffusiondet: Diffusion model for object detection," in *ICCV*, 2023.
- [72] H. Zhang *et al.*, "Dino: Detr with improved denoising anchor boxes for end-to-end object detection," in *ICLR*, 2023.
- [73] S. Zhang *et al.*, "Dense distinct query for end-to-end object detection," in *CVPR*, 2023.
- [74] Y. Dai *et al.*, "Attentional local contrast networks for infrared small target detection," *TGRS*, 2021.
- [75] Y.-T. Chen *et al.*, "Multimodal object detection via probabilistic ensembling," in *ECCV*, 2022.
- [76] X. He *et al.*, "Multispectral object detection via cross-modal conflict-aware learning," in *ACM MM*, 2023.
- [77] Y. Kondo *et al.*, "MVA2023 Small Object Detection Challenge for Spotting Birds: Dataset, Methods, and Results," in *CVPR*, 2023.
- [78] Y. Dai *et al.*, "One-stage cascade refinement networks for infrared small target detection," *TGRS*, 2023.
- [79] H. Sun *et al.*, "Receptive-field and direction induced attention network for infrared dim small target detection with a large-scale dataset irdst," *TGRS*, 2023.
- [80] G. Chen *et al.*, "A survey of the four pillars for small object detection: Multiscale representation, contextual information, super-resolution, and region proposal," *TSMC*, 2022.

- [81] Y. Chen *et al.*, "Scale-aware automatic augmentation for object detection," in *CVPR*, 2021.
- [82] M. Kisantal *et al.*, "Augmentation for small object detection," *ArXiv*, 2019.
- [83] J. Han *et al.*, "Redet: A rotation-equivariant detector for aerial object detection," in *CVPR*, 2021.
- [84] T.-Y. Lin *et al.*, "Feature pyramid networks for object detection," in *CVPR*, 2017.
- [85] Y. Gong *et al.*, "Effective fusion factor in fpn for tiny object detection," in *WACV*, 2021.
- [86] B. Singh *et al.*, "Sniper: Efficient multi-scale training," *NeurIPS*, 2018.
- [87] S. Bell *et al.*, "Inside-outside net: Detecting objects in context with skip pooling and recurrent neural networks," in *CVPR*, 2016.
- [88] X. Tang *et al.*, "Pyramidbox: A context-assisted single shot face detector," in *ECCV*, 2018.
- [89] C. Deng *et al.*, "Extended feature pyramid network for small object detection," *TMM*, 2021.
- [90] P. Zhou *et al.*, "Scale-transferrable object detection," in *CVPR*, 2018.
- [91] J. Noh *et al.*, "Better to follow, follow to be better: Towards precise supervision of feature super-resolution for small object detection," in *ICCV*, 2019.
- [92] Y. Bai *et al.*, "Sod-mtgan: Small object detection via multi-task generative adversarial network," in *ECCV*, 2018.
- [93] J. Rivest *et al.*, "Detection of dim targets in digital infrared imagery by morphological image processing," *Opt. Eng.*, 1996.
- [94] Deshp *et al.*, "Max-mean and max-median filters for detection of small targets," in *SDPST*, 1999.
- [95] C. P. Chen *et al.*, "A local contrast method for small infrared target detection," *TGRS*, 2013.
- [96] J. Han *et al.*, "Infrared small target detection utilizing the multiscale relative local contrast measure," *GRSL*, 2018.
- [97] S. Moradi *et al.*, "A false-alarm aware methodology to develop robust and efficient multi-scale infrared small target detection algorithm," *Infrared Phys. Techn.*, 2018.
- [98] J. Han *et al.*, "Infrared small target detection based on the weighted strengthened local contrast measure," *GRSL*, 2020.
- [99] J. Han *et al.*, "A local contrast method for infrared small-target detection utilizing a tri-layer window," *GRSL*, 2019.
- [100] Y. Dai *et al.*, "Reweighted infrared patch-tensor model with both nonlocal and local priors for single-frame small target detection," *JSTAR*, 2017.
- [101] L. Zhang *et al.*, "Infrared small target detection via non-convex rank approximation minimization joint  $l_2$ ,  $l_1$  norm," *RS*, 2018.
- [102] T. Liu *et al.*, "Non-convex tensor low-rank approximation for infrared small target detection," *TGRS*, 2021.
- [103] L. Zhang *et al.*, "Infrared small target detection based on partial sum of the tensor nuclear norm," *RS*, 2019.
- [104] Y. Sun *et al.*, "Infrared dim and small target detection via multiple subspace learning and spatial-temporal patch-tensor model," *TGRS*, 2020.
- [105] M. Zhang *et al.*, "Rkformer: Runge-kutta transformer with random-connection attention for infrared small target detection," in *ACM MM*, 2022.
- [106] M. Zhang *et al.*, "Exploring feature compensation and cross-level correlation for infrared small target detection," in *TW ACM MM*, 2022.
- [107] M. Ju *et al.*, "Istdet: An efficient end-to-end neural network for infrared small target detection," *Infrared Phys. Techn.*, 2021.
- [108] Q. Hou *et al.*, "Ristdnet: Robust infrared small target detection network," *GRSL*, 2021.
- [109] D. Pang *et al.*, "Sttm-sfr: Spatial-temporal tensor modeling with saliency filter regularization for infrared small target detection," *TGRS*, 2022.
- [110] T. Liu *et al.*, "Nonconvex tensor low-rank approximation for infrared small target detection," *TGRS*, 2021.
- [111] Y. Zhang *et al.*, "Learning nonlocal quadrature contrast for detection and recognition of infrared rotary-wing uav targets in complex background," *TGRS*, 2022.
- [112] J. Du *et al.*, "A spatial-temporal feature-based detection framework for infrared dim small target," *TGRS*, 2021.
- [113] S. Hwang *et al.*, "Multispectral pedestrian detection: Benchmark dataset and baselines," in *CVPR*, 2015.
- [114] M. Yuan *et al.*, "Translation, scale and rotation: cross-modal alignment meets rgb-infrared vehicle detection," in *ECCV*, 2022.
- [115] Y.-T. Chen *et al.*, "Multimodal object detection via probabilistic ensembling," in *ECCV*, 2022.
- [116] H. Zhang *et al.*, "Multispectral fusion for object detection with cyclic fuse-and-refine blocks," in *ICIP*, 2020.
- [117] Y. Zhang *et al.*, "When pedestrian detection meets multi-modal learning: Generalist model and benchmark dataset," in *ECCV*, 2024.
- [118] C. Li *et al.*, "Multispectral pedestrian detection via simultaneous detection and segmentation," in *BMVC*, 2018.
- [119] L. Zhang *et al.*, "Weakly aligned cross-modal learning for multispectral pedestrian detection," in *ICCV*, 2019.
- [120] J. U. Kim *et al.*, "Towards versatile pedestrian detector with multisensory-matching and multispectral recalling memory," in *AAAI*, 2022.
- [121] C. Chen *et al.*, "Weakly misalignment-free adaptive feature alignment for uavs-based multimodal object detection," in *CVPR*, 2024.
- [122] D. Guan *et al.*, "Fusion of multispectral data through illumination-aware deep neural networks for pedestrian detection," *IF*, 2019.
- [123] Y. Zhang *et al.*, "Illumination-guided rgbt object detection with inter-and intra-modality fusion," *TIM*, 2023.
- [124] Q. Xu *et al.*, "Heterogeneous graph transformer for multiple tiny object tracking in rgb-t videos," *TMM*, 2024.
- [125] H. Rezafofighi *et al.*, "Generalized intersection over union: A metric and a loss for bounding box regression," in *CVPR*, 2019.
- [126] Z. Zheng *et al.*, "Distance-iou loss: Faster and better learning for bounding box regression," in *AAAI*, 2020.
- [127] Z. Zhang, "Flexible camera calibration by viewing a plane from unknown orientations," in *ICCV*, 1999.
- [128] Z. Zhang, "A flexible new technique for camera calibration," *TPAMI*, 2000.
- [129] L. Wang *et al.*, "Parallax attention for unsupervised stereo correspondence learning," *TPAMI*, 2020.
- [130] D. Programmer, "Darklabel," <http://darkpgmr.tistory.com/16>, 2022.
- [131] H. Xie *et al.*, "Prcl: Probabilistic representation contrastive learning for semi-supervised semantic segmentation," *IJCV*, 2024.
- [132] K. Chen *et al.*, "MMDetection: Open mmlab detection toolbox and benchmark," *ArXiv*, 2019.
- [133] K. He *et al.*, "Deep residual learning for image recognition," in *CVPR*, 2016.
- [134] Y. Xinyi *et al.*, "Basicirstd," <https://github.com/XinyiYing/BasicIRSTD>, 2021.
- [135] P. Sun *et al.*, "Sparse r-cnn: End-to-end object detection with learnable proposals," in *CVPR*, 2021.